MNRAS 000, 1–20 (2021) Preprint 2 September 2022 Compiled using MNRAS LATEX style file v3.0

Early-time spectroscopic modelling of the 1986G-like SN Ia SN 2021rhu with TARDIS

L. Harvey,[1]★
[1]School of Physics, Trinity College Dublin, The University of Dublin, Dublin 2, Ireland

Accepted XXX. Received YYY; in original form ZZZ

ABSTRACT

We present the spectroscopic modelling of the 1986G-like transitional supernova Ia SN 2021rhu from -12.2d until 0.6d with respect to maximum brightness using the radiative-transfer spectral-synthesis code TARDIS. This modelling work was initially completed using the density profile from the delayed detonation N100 model. We subsequently present a method of projecting the derived abundance profile onto another density profile, in turn using this method to produce custom models for SN 2021rhu with density profiles arising from the double detonation scenario (M0803 & M0905) as well as a pure deflagration (W7). Due to the low densities in the outer regions, we show the W7 density profile to be inadequate as SN 2021rhu exhibits high velocities in the calcium H&K feature. This goes against conclusions from a previous study on the modelling of SN 1986G itself. We present a similar method for projecting an abundance profile to higher luminosities in order to match observed spectra with large corrections for host extinction. With the sizable uncertainties on the extent to which the observations of SN 2021rhu are impacted by extinction from the host galaxy, we use this second projection method to produce a model which accounts for this host extinction. This allows us to place limits on the abundances of the species involved, in turn giving us the chance to compare to models from the literature. We rule out double-detonation and violent merger mechanisms, concluding that the resulting abundances lie somewhat in line with the delayed detonation models.

Key words: keyword 1 – keyword 2 – keyword 3

1 INTRODUCTION

Famed for their use as distance indicators, Type Ia supernovae (SNe Ia) are the thermonuclear explosions of CO white dwarfs arising from interactions with a binary companion. Standardisable through the relationship between their peak luminosity and light curve width (Pskovskii 1977; Phillips 1993) they have been integral to the field of cosmology; leading to the discovery of the accelerating expansion of the Universe (Riess et al. 1998; Perlmutter et al. 1999) and in turn the theoretical prediction of dark energy. Their power as standard candles is predicated upon their obedience to this standardisation relation, however as the sample grows it is becoming more diverse in nature. Whether these outlying transients are produced by different progenitor channels and/or explosion scenarios remains to be seen, however by studying the various subclasses through spectroscopic and photometric modelling we aim to better understand this scatter and thus improve the power of SNe Ia as distance indicators.

SN 1986G was the first of these 'disobedient' supernovae to cast doubt upon the usefulness of SNe Ia as standard candles (Phillips et al. 1987; Ashall et al. 2016). Appearing subluminous for its Δm_{15} - B band luminosity decrease in the 15 days post peak - it now lies in the transitional region of the parameter space between the normal SNe Ia and the 91bg-like subclass.

Compared to the sky surveys and spectroscopic follow-up operations in place today, the world of observational astronomy was a different place 35 years ago and as such the spectral data coverage for SN 1986G only begins 3 days before maximum light. Due to this delay, substantial amounts of information about the higher velocity material is missed and the spectroscopic modelling carried out by Ashall et al. (2016) was restricted to the lower velocity ejecta. With the high-cadence photometric observations of the Zwicky Transient Facility (ZTF), an analogue to SN 1986G was found in the nearby supernova SN 2021rhu (ZTF21abiuvdk) at a matter of hours past first light. This was key in triggering the follow-up of the object with a variety of telescopes and programs, making for the high cadence spectroscopic series presented and explored here.

As a thermonuclear supernova in a nearby galaxy with a TRGB distance measurement, SN 2021rhu was used by Dhawan et al. (2022) as a distance ladder calibrator object for a measurement of H_0. This has also been the case with other such transitional objects in the past, with SN 2011iv standing as one of the calibrator supernovae for the recent SH0ES H_0 measurement (Riess et al. 2021). In this case the calibrator objects were required to pass cuts on colour ($|c| < 0.15$) and stretch ($|x1| < 2$) to be determined adequate for calibration, with a fellow transitional object SN 2007on being excluded with $x1 = -2.2$. With these transitional supernovae appearing subluminous and spectroscopically different to their normal counterparts, it remains an open question as to whether they arise from the same, single progenitor channel and by extension, can they truly be cosmologically useful as calibrator targets.

★ E-mail: luharvey@tcd.ie

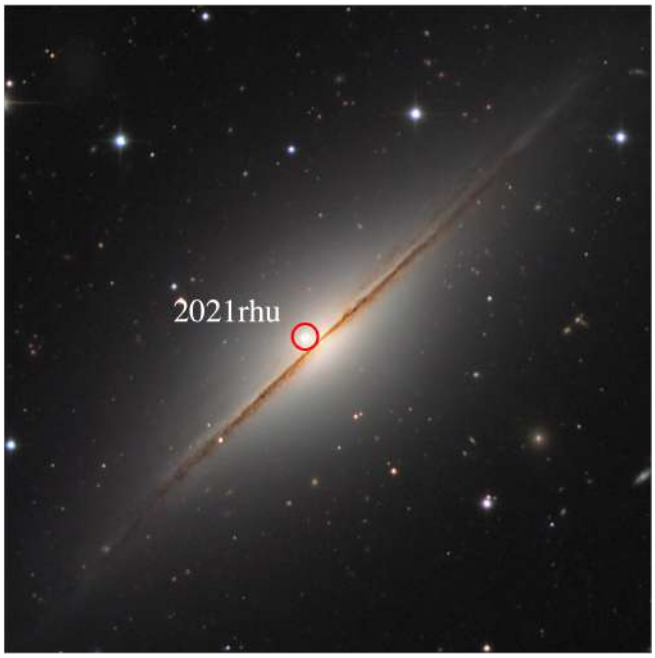

Figure 1. Host galaxy NGC7814 showing SN 2021rhu in the red circle just outside the plane of the galaxy in the region of the bulge. *Credit: Prompt 7 CTIO/UNC Chile, Chart32-Team.*

The aim of the modelling process for SN 2021rhu is to constrain the abundances of key elements through abundance tomography which could provide clues as to the explosion mechanism at play; namely the abundance of titanium required to produce the observed evolution of the strong feature seen in the spectra at ~4300Å. Due to the enhanced production of titanium, the double detonation mechanism is an interesting avenue of investigation in the context of lower luminosity thermonuclear events with strong Ti II absorption in the past. It has been discussed however that instead of higher titanium production, lower ejecta temperatures are responsible for this increased absorption (Mazzali et al. 1997; Nugent et al. 1995). Being the result of absorption from singly ionised titanium, this feature weakens at higher ejecta temperatures as most of the titanium is hidden away in higher ionisation states.

In Section 2 we present the observational data followed by the spectroscopic modelling in Section 3 and finally a discussion of the conclusions in Section 6.

2 OBSERVATIONS

SN 2021rhu was discovered on 20210701 (Modified Julian Date, MJD of 59396.56) at 15.6623 mag in the ZTF*r*-band by the ALeRCE group (Carrasco-Davis et al. 2020) with the ZTF camera mounted on the 48 inch Samuel Oschin telescope (P48) at the Palomar observatory. At RA 00:03:15.42, Dec +16:08:44.51, this thermonuclear supernova was found just outside the plane of the edge-on spiral galaxy NGC 7814 at a redshift of z = 0.003506 (Springob et al. 2005). The Type Ia classification was drawn from the ALeRCE spectrum taken July 2nd 2021 (MJD 59396.94) (Atapin et al. 2021) with the Transient Double-beam Spectrograph on the 2.5m telescope of the Caucasus Mountain Observatory (Potanin et al. 2020). Identified as an interesting object due to its low redshift and early discovery, an extensive monitoring campaign was initiated.

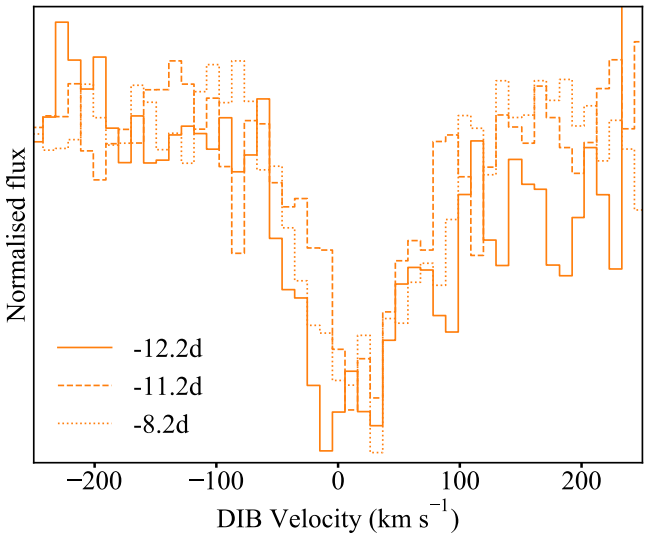

Figure 2. The diffuse interstellar band seen in the high resolution XShooter spectra at epochs of -12.2d, -11.2d, and -8.2d with respect to peak. The equivalent width measurement of this feature gives the estimate of the extent to which the data is affected by hosted extinction.

2.1 Distance and extinction towards SN 2021rhu

Due to the proximity of the host galaxy to the Milky Way, SN 2021rhu doesn't truly lie in the Hubble flow and as such a redshift-independent distance is required. There exists a range of distance measurements from previous works for the host galaxy of SN 2021rhu. Here we adopt the updated tip of the red-giant branch (TRGB) measurement of $\mu = 30.86 \pm 0.07$ from Dhawan et al. (2022) in which they used SN 2021rhu as a calibrator object for their measurement of H_0.

The SN 2021rhu photometry was corrected for Milky Way extinction in accordance with the dust extinction model from Fitzpatrick & Massa (2007) with $R_V = 3.1$ and $E(B-V) = 0.0383 \pm 0.0003$, as taken from Schlegel et al. (1998) accessed through the PYTHON package ASTROQUERY (Ginsburg et al. 2019).

With regards to host extinction, we turn to the high resolution XShooter spectra - of which there are three, discussed in Section 2.4 - to gauge an estimate of the contribution of dust attenuation from the local environment. We measure the equivalent width of the diffuse interstellar band (see Fig. 2) which has been shown to display a loose correlation with host A_V by Phillips et al. (2013a), with a 1σ dispersion in this relation of 50%. We measure a value of 80±1mÅ which corresponds to a host extinction of $A_V = 0.42 \pm 0.21$mag. Lying just out of the plane of the host galaxy NGC 7814 as seen in Fig. 1, this potentially large host extinction is not to be unexpected.

In terms of progressing with the analysis of the object and in turn the spectroscopic modelling, we choose to initially disregard this host extinction to create a base model. In turn we create a new model with the inclusion of host extinction. This will allow us to set lower and upper limits on each of the elemental abundances depending upon the true level of host extinction.

2.2 Photometry

After discovery, daily *g r* and *i* band photometry was triggered by the ZTF group on the P48 telescope, leading to very high cadence light curves in the three ZTF bands over the supernova's evolution. The photometric data presented here for SN 2021rhu is the result of

the ztffps forced photometry pipeline (Reusch 2020). Three epochs of Swift UVOT *u* measurements were also obtained. The Swift data were reduced... The unextinction-corrected photometric data for SN 2010rhu can be found in Table A1. K corrections have not been applied due to the low redshift of z = 0.003506.

The absolute magnitude light curves of SN 2021rhu are shown in Fig. 3 along with the *UBVRI* photometry for the transitional event, SN 1986G (Phillips et al. 1987) and for the well studied normal Type Ia SN 2011fe (Richmond & Smith 2012; Munari et al. 2013; Brown et al. 2014). The photometric data for SN 1986G and SN 2011fe were retrieved through the Open Supernova Catalog (Guillochon et al. 2017). We have corrected both their light curves for MW extinction and converted to absolute magnitude (see Table A2 for values and their associated references). Host extinction for the SN 1986G must also be accounted for as it is known to have occurred in a dust lane of its host galaxy Centaurus A (Phillips et al. 1987) and as such exhibits large amounts of reddening. Phillips et al. (2013b) measured the column densities of this neutral sodium and potassium from high dispersion spectra for both the MW and host absorption components to determine the extent of extinction (see values in A2).

2.3 Light-curve properties

As evident in the *B* and *V* photometry from Fig. 3, SN 1986G is subluminous when compared against the normal objects in the Ia class. This also appears to be the case for SN 2021rhu as seen in the comparisons between its *ri* photometry and the *RI* photometry available for SN 2011fe. We note that although the response functions of the *ri* and *RI* filters differ slightly, this only leads to a magnitude difference on the order of 0.05mag and as such this luminosity comparison is still significant.

The SN 2021rhu photometry was fit by Dhawan et al. (2022) using the light-curve fitter SALT2 (Guy et al. 2007) as accessed through `sncosmo` (Barbary et al. 2016). This fit was performed solely on the ZTF*g* and ZTF*r* data as SALT2 is not well defined at wavelengths redward of 7000Å. The date of maximum light was fit as $t_0 = 59410.60 \pm 0.04$.

With SALT2 parameters of $x_1 = -2.074 \pm 0.025$ and $c = 0.054 \pm 0.028$, SN 2021rhu satisfied the criteria of $|x_1| < 3$ and $|c| < 0.3$ as laid out in Dhawan et al. (2022) as typical cosmological cuts. It was argued that despite the low x_1 value - also seen in other peculiar, fast-decliners - the clear *r* shoulder and *i* secondary maximum are characteristic of normal and transitional SNe Ia that have been used for cosmology. They went a step further by calculating the colour-stretch parameter through another light-curve fitter SNooPY as $s_{BV} = 0.72$ which is consistent with normal and transitional thermonuclear events.

The resulting time-varying SED was then integrated through different filters to produce the extrapolated light-curves for each of the other photometric bands, seen as solid lines in Fig 3. While SN 2021rhu appears subluminous in comparison to SN 2011fe, it also exhibits a faster decline and as such it is necessary to examine where it lies in the parameter space of the Phillips relation in order to determine the extent to which it strays from other thermonuclear events.

From the extrapolated *B* light-curve taken from the SALT2 fit we measure the peak magnitude as $M_B = -18.6 \pm 0.2$ with $\Delta m_{15} = 1.53 \pm 0.2$. As seen in Fig. 4, these values put SN 2021rhu slightly below the Phillips relation, in the subluminous region of the parameter space. At a similar distance from the luminosity-width relation as its faster evolving analogue SN 1986G, SN 2021rhu appears to be a transitional transient.

The precise position of SN 2021rhu in Fig. 4 is uncertain due

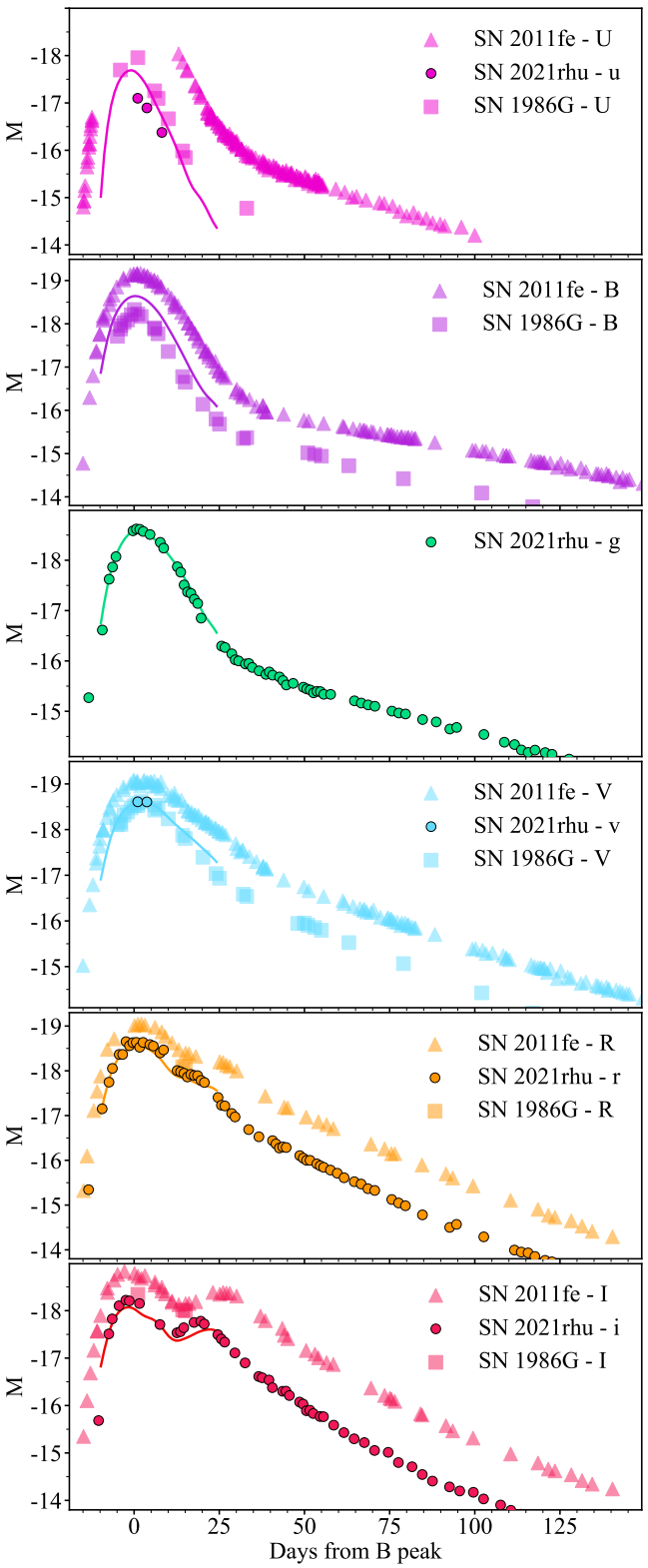

Figure 3. Absolute magnitude light curves for SN 2021rhu in the Swift *u* and ZTF *g*, *r*, and *i* bands compared with the *BVRI* photometry of the normal SN 2011fe and the *BVRI* photometry of SN 1986G. The SALT fits to SN 2021rhu are displayed for the *ugri* bands. The SALT light-curves calculated from the fitted SED in the B and V bands are also displayed for comparison to the other two objects. This extrapolated B band light-curve is the source of the peak M_B and $\Delta m_{B,15}$ measurements for SN 2021rhu seen in Fig. 4.

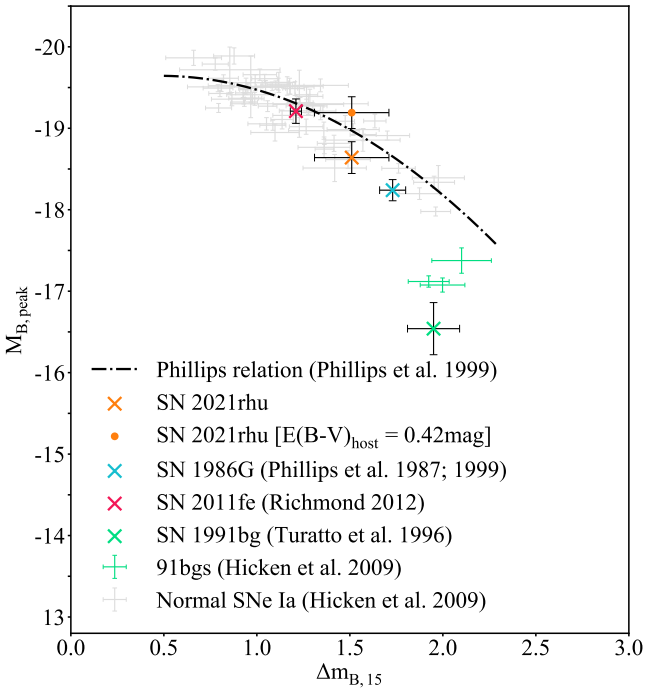

Figure 4. Locations of SN 1991bg, SN 1986G, SN 2021rhu, and SN 2011fe in the parameter space of the Phillips relation. As evident from its intermediate location between SN 2011fe and the transitional SN 1986G, SN 2021rhu lives below the Phillips relation however photometrically closer than SN 1986G to the normal objects in the class. The equation for the Phillips relation is taken from Phillips et al. (1999).

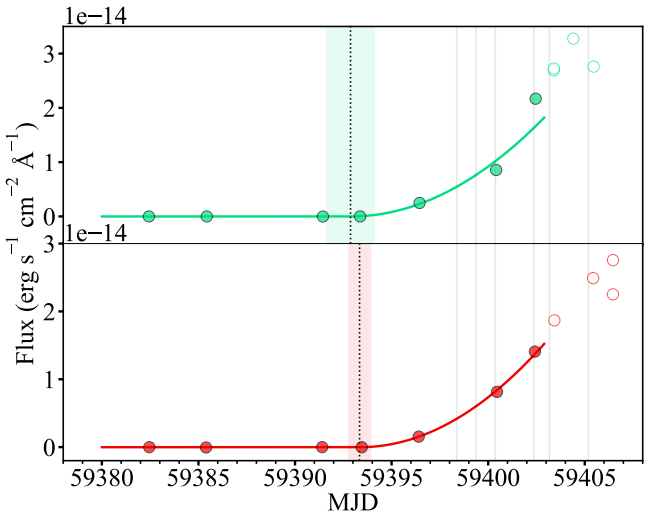

Figure 5. Results of the fitting of the ZTF*g* (top) and ZTF*r* (bottom) light-curve rises with Equation 1. The fitted date of first light is indicated by the black dotted lines with the shaded regions representing the 1σ uncertainties. The grey vertical lines mark the dates of spectral epochs.

to the fact that SALT2 is trained upon normal SN Ia spectra which do not exhibit the signature Ti II feature seen in SN 2021rhu and SN 1986G. The extrapolated *B* photometry involves integrating over the wavelength region in which this feature occurs and as such the magnitudes in *B* may be overestimated.

If we were to include the mean from the $A_V = 0.42 \pm 0.21$mag host extinction measurement, SN 2021rhu would be positioned up above the Phillips relation. As this strong Ti II trough has only been previously seen in subluminous objects, we take this mean of 0.42mag as the host extinction upper limit.

To obtain a date of first light, we employed the prescription from Miller et al. (2020) in which the early light-curve rise up to ~ 40% of the peak magnitude can be fit in flux space with the following power law:

$$f(t) = C + H[t_{\rm fl}]A(t - t_{\rm fl})^{\alpha}. \quad (1)$$

Here $t_{\rm fl}$ is the time of first light, α is the power law index, A is the proportionality constant, C is a constant offset, and $H[t_{\rm fl}]$ is the Heaviside function taking the value 0 before $t = t_{\rm fl}$ and 1 afterwards. The 40% cutoff as used by Miller et al. (2020) was noted to be an arbitrary choice and as such we included datapoints up to 50% of the peak flux. The date for first light was taken as a weighted mean of the results of fitting the ZTF*g* and ZTF*r* separately to be 59393.19 ± 0.25d, making for a rise time of 17.41 ± 0.25d. In previous studies the power law index has been fixed as $\alpha = 2$ with the luminosity scaling with the expanding fireball surface area. When left as a free parameter, the resulting value can provide insight as to the distribution of ^{56}Ni. Smaller values of α describe a more gradual rise and point towards a more extended ^{56}Ni distribution with a shorter time between explosion and first light (dark phase), whereas a large index implies a lesser degree of mixing with the ^{56}Ni restricted to the core and all the photons escaping over the course of a smaller time frame following a longer dark phase (Firth et al. 2015). The fitted values of α were 2.00 ± 0.58 for ZTF*g* and 2.01 ± 0.25 for ZTF*r*.

2.4 Spectroscopy

Spectra were obtained for SN 2021rhu from −12 to +98 d with respect to peak brightness at a number of facilities: the XShooter spectrograph (Vernet et al. 2011) on the ESO Very Large Telescope (VLT), the Spectral Energy Distribution Machince (SEDM) (Blagorodnova et al. 2018) on the automated P60 (Cenko et al. 2006) at the Palomar observatory, the Spectrograph for the Rapid Acquisition of Transients (SPRAT) (Piascik et al. 2014) at the Liverpool Telescope (LT) (Steele et al. 2004), and the Alhambra Faint Object Spectrograph and Camera (ALFOSC) on the Nordic Optical Telecsope (NOT). The observational details for the spectra are given in Fig. A3.

Data reduction for the XShooter spectra were performed following the method in Maguire et al. (2016) that uses the REFLEX pipeline (Modigliani et al. 2010; Freudling et al. 2013). The SEDM spectra were reduced through the IFU pipeline developed by Rigault et al. (2019). The SPRAT spectra were reduced through PYRAF using a custom PYTHON script following Prentice et al. (2021). Finally, the ALFOSC NOT reductions employed the standard routines in IRAF.

Absolute flux calibration of the spectra was carried out using the ZTF*g* and ZTF*r* bands as not only do they have a higher cadence than the ZTF*i* photometry, many of the spectra do not possess a wavelength range that covers the ZTF*i* filter response function in its entirety. Synthetic photometry measurements were calculated from the spectra using the PYPHOT package (Fouesneau 2022) and then compared to the photometry values - if coinciding with the epoch of the spectrum - or an interpolated light curve. This interpolated light curve was comprised of a power law fit for the rise and an exponentially modified Gaussian for the main body of the light curve. These comparisons resulted in calibration factors for each of the two bands

at their corresponding effective wavelengths. Fitting a linear function to these calibration factors resulted in a wavelength dependant calibration function which could then be applied to calibrate the spectra to the photometry. We note that this style of calibration can cause scaling issues with the spectrum in regions far away from the effective wavelengths of the filters, however as these filters cover almost the entire range in which we are interested, this has an insignificant impact on the spectra presented here.

The spectra are subsequently corrected to the restframe using the redshift of the host galaxy, for extinction using the MW values, and to luminosity using the TRGB distance modulus, all given in Table A2.

2.5 Observed spectral properties

In Fig. 6 we present the spectral series for SN 2021rhu, shown alongside some of the available spectra for SN 1986G (Cristiani et al. 1992) with similar epochs for comparison. The spectra of SN 2021rhu have only been corrected for MW extinction. In such a side-by-side comparison the resemblance between the two transients can be seen, with the only notable difference between the two being a slightly lower Si II $\lambda\lambda$6355 velocity in SN 1986G.

Figure 7 compares the maximum-light spectrum of SN 2021rhu to that of SN 2011fe, SN 1986G and SN 1991bg - the namesake of the subluminous 91bg-like subclass of thermonuclear transients (Filippenko et al. 1992; Leibundgut et al. 1993; Turatto et al. 1996). The titanium feature seen in the SN 1991bg spectrum at ~4300Å is common to the subclass and can also be seen clearly in SN 1986G and SN 2021rhu although to a less pronounced extent. This feature is absent in SN 2011fe (Parrent et al. 2012) as it is in all the so-called normal SNe Ia. The presence of this absorption feature, along with having a brightness at peak between the normal and 91-bg like Ias, gives SN 1986G and SN 2021rhu their 'transitional' classification.

The velocity evolution of the principle Si II feature at $\lambda\lambda$6355 is measured here for SN 1991bg , SN 2011fe (SPEC REF), and SN 2021rhu, with the results seen in Fig 8 against the values measured for SN 1986G in Phillips et al. (1987). SN 2021rhu velocities are consistently higher than the velocities seen at similar epochs in SN 2011fe by $\sim$ 2000 km s^{-1}, lying slightly higher - but roughly consistent with - SN 1986G.

Visible in all three high resolution XShooter spectra - as well as the -10.2d SEDM spectrum - is a small feature to the red of the principle silicon feature. The feature in this region is typically associated with carbon, specifically the C II λ6380 line. If this feature is formed by this singly ionised carbon it resides at $\sim$ 10000 km s^{-1}at -12.2d which is far below the 15898 $\pm$ 100 km s^{-1}velocity of the Si II $\lambda\lambda$6355 line at this epoch. As the silicon velocity typically traces the velocity of the photosphere in the pre-peak regime, this carbon feature - if formed by C II λ6380 - exists at velocities some 6000 km s^{-1}slower than the photosphere. A potential formation scenario would have some slower moving carbon, while still at explosive velocities, geometrically further out than the photosphere at these early epochs. The C II λ7236 feature also appears to be present with a slightly higher velocity of $\sim$ 11000 km s^{-1}in the -12.2d spectrum, lending credence to the idea that slow moving C II above the photosphere could be responsible for these features. The modelling of these carbon features is not pursued in this paper.

3 SPECTRAL MODELLING

In this section we describe the Tardis code used to model the spectra, present the density profiles which we shall be exploring, and introduce a couple of methods to manipulate models to difference density profiles and input parameters.

The key difference between the previous spectral modelling work of Ashall et al. (2016) for SN 1986G and the modelling discussed here is the ability of the data to constrain the higher velocity material. The earliest spectrum available for SN 1986G was recorded just 3d before maximum light in comparison to 11.9d for SN 2021rhu. With five additional SN 2021rhu spectra taken in this ~9d window we are able to better constrain the composition of material in the regions of the ejecta above $\sim$ 15000 km s^{-1}.

3.1 Tardis

Tardis is an open-source Monte-Carlo radiative-transfer spectral synthesis code for one-dimensional models of transients (Kerzendorf & Sim 2014; Kerzendorf et al. 2020). Written originally for use with SNe Ia and their various subclasses (Barna et al. 2017; Magee et al. 2021), it has since been applied to study a wide range of astrophysical transients from stripped core-collapse SNe (Williamson et al. 2021) to kilonovae (Smartt et al. 2017; Gillanders et al. 2021, 2022a).

Tardis operates by propagating photon packets through a specified ejecta and calculating the interactions with the material to synthesise a spectrum. This process is repeated multiple times with a low packet count to converge the temperature of the blackbody from which to sample the photon wavelengths. In the final iteration this packet number is increased dramatically - from 40,000 to 1,000,000 in the case of this work - for the final iteration in which the synthetic spectrum is calculated. Accompanying this packet number increase is the introduction of virtual packets. These virtual packets are duplicates of the real packets which are created in interactions with the ejecta. This is included to boost the signal to noise of the resulting spectrum.

These initial packet wavelengths are sampled from this blackbody distribution and released from an opaque inner boundary which represents the photosphere in the homologously expanding plasma. As time progresses and the densities fall, this boundary in the expanding material will recede inwards to reveal slower moving ejecta. It is upon this fact that the method of abundance tomography is built; each successive spectrum will have a slightly lower photospheric velocity and will therefore be constraining the abundances of this newly revealed matter.

Spectra synthesised by Tardis cover a range of wavelength domains, and as such this creates issues with the validity of the photospheric approximation (Gillanders et al. 2022b). Photons of different frequencies probe to different optical depths in a plasma and therefore experience photospheres at different locations. The simplification of the system to a single fixed photosphere across the spectrum results in a flux excess seen in the redder wavelengths, however the absorption features still show through.

Another discussion point in terms of validity is the lack of treatment of radioactive decay, as the luminosity in a SN Ia is driven by the decay of ^{56}Ni to ^{56}Co. This energy injection is encoded in the blackbody emission from the photosphere, however the energy from the decaying ^{56}Ni in the ejecta above the photosphere is not incorporated. The negative impact of this approximation is insignificant whilst the bulk of this radioactive material lies below the photosphere and thus the code produces synthetic data in agreement with observations up until several days after peak (Kerzendorf & Sim 2014).

3.2 Density profiles

In the context of SN 2021rhu, we investigated four different density profiles arising from three different explosion mechanisms (Fig. 9).

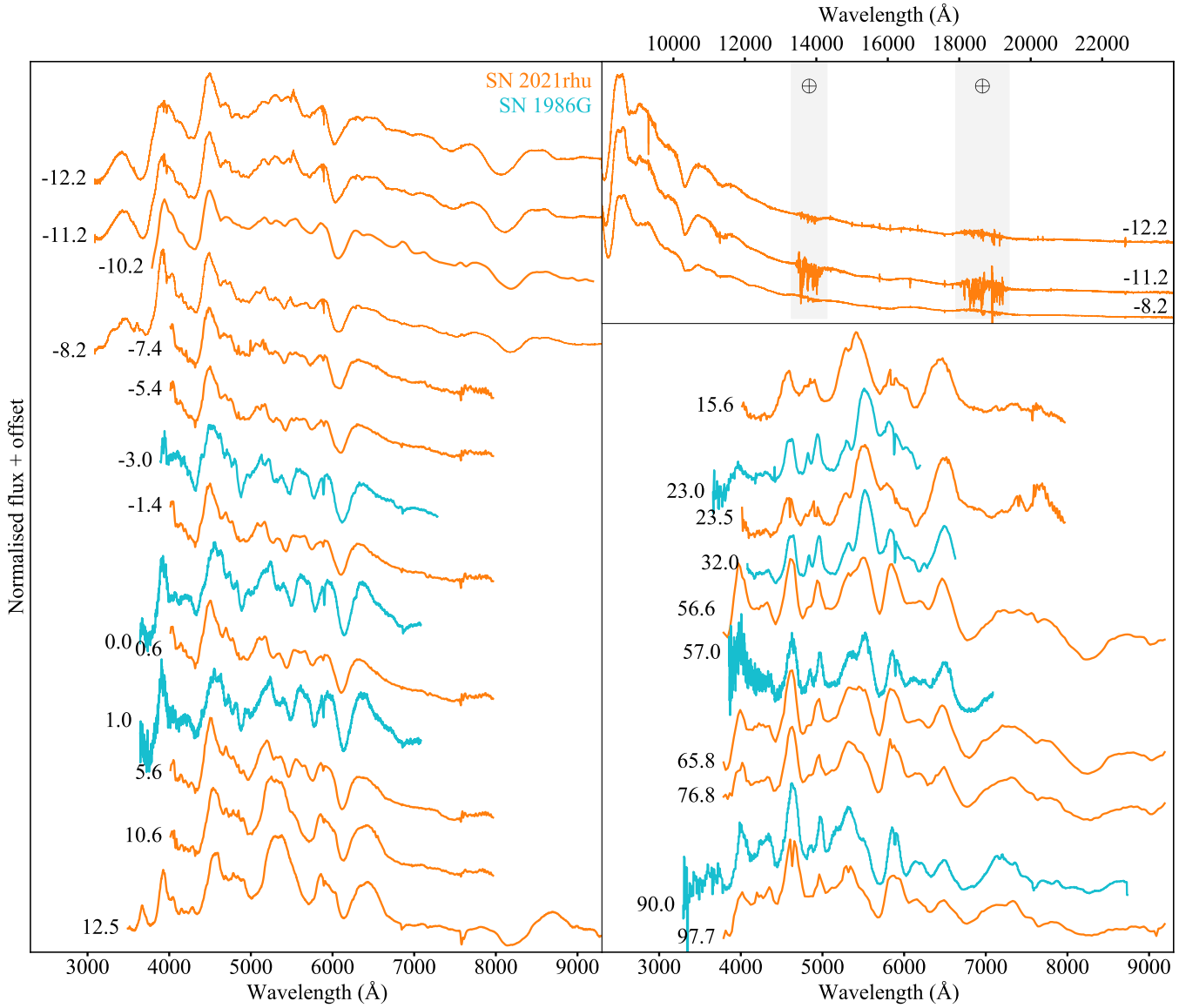

Figure 6. Spectral data for SN 2021rhu (orange) compared against the spectral evolution of SN 1986G (blue). The phases of each spectrum relative to peak are displayed alongside each spectrum in days. All spectra have been corrected for redshift and extinction, in the case of SN 1986G this extinction correction included both a MW component as well as a component to compensate for the host dust lane. The details of the SN 2021rhu can be seen in tables A3. The panel to the top right shows the infrared region of the three XShooter epochs for SN 2021rhu.

Firstly we considered the delayed-detonation N100 density profile (Röpke et al. 2012; Seitenzahl et al. 2013), which results from an initial deflagration phase causing the white dwarf to swell before becoming a detonation. Secondly we looked at two density profiles from double-detonation explosion models, M0803 and M0905 Gronow et al. (2021), which are similar to the Sub-Chandrasekhar profile chosen by Ashall et al. (2016). The final density profile chosen was the W7 arising from a fast-deflagration model. We also discuss the plausibility of W7e0.7 which is the W7 model scaled down to 70% the kinetic energy through the following equations.

$$\rho' = \rho_0 \left(\frac{E'}{E_0}\right)^{-\frac{3}{2}} \left(\frac{M'}{M_0}\right)^{\frac{5}{2}}, \quad (2)$$

$$v' = v_0 \left(\frac{E'}{E_0}\right)^{\frac{1}{2}} \left(\frac{M'}{M_0}\right)^{-\frac{1}{2}}. \quad (3)$$

where ρ is the density profile, E is the kinetic energy, v is the velocity profile, and M is the mass. The initial values are denoted with subscript 0, with the new values indicated by dashes.

The modelling work of SN 1986G by Ashall et al. (2016) concluded this scaled W7 density profile to be the preferred choice, with the kinetic energy matching the explosion energy calculated from the derived abundance profile. They also found their sub-Chandrasekhar density profile to be insufficient as it required oxygen probing to deeper layers in the ejecta than sulphur which is in direct conflict with nucleosynthetic calculations.

As the spectral data available for SN 1986G only commenced 3d

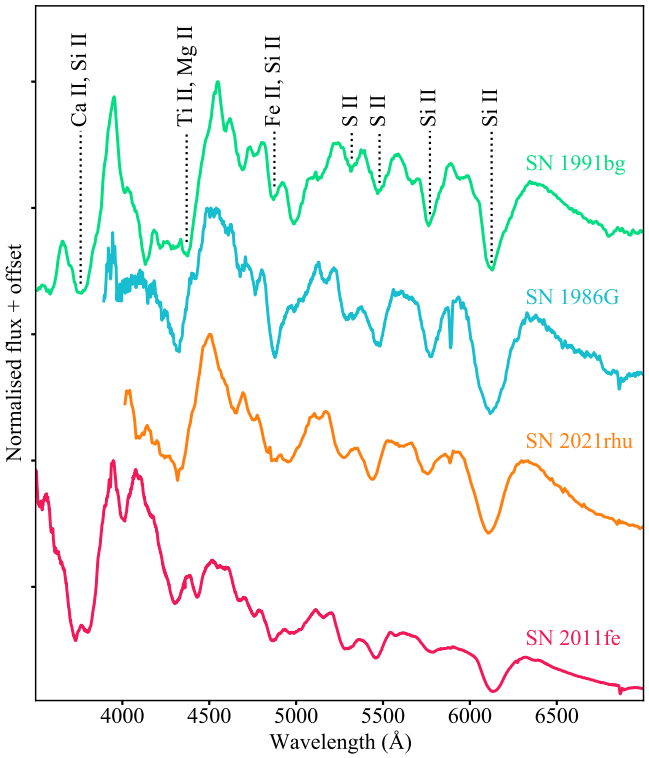

Figure 7. Comparison between the peak time spectra of SN 1991bg, SN 1986G, SN 2021rhu and SN 2011fe. Key lines for the thermonuclear transients are labelled along with the strong titanium feature at 4300Å seen in SN 1991bg, SN 1986G, and SN 2021rhu that does not appear in the normal events of the class.

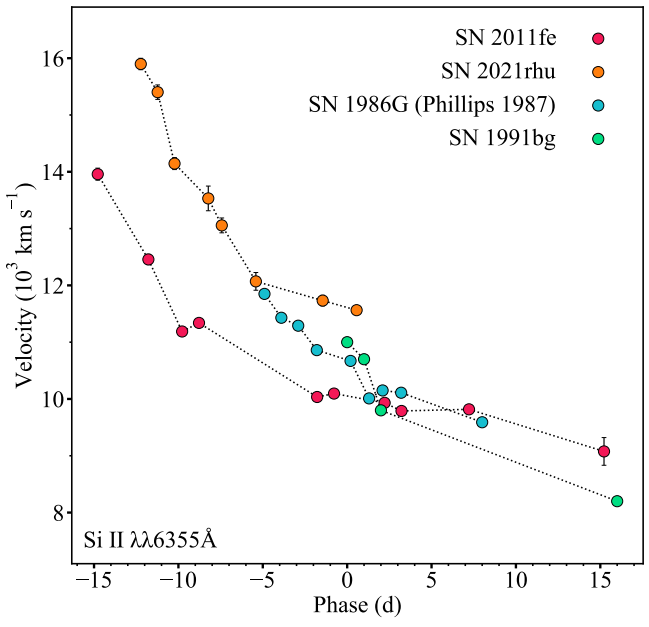

Figure 8. Velocity evolution of the principle Si II feature measured here for SN 2021rhu, SN 2011fe (Parrent et al. 2012), and SN 1991bg (Filippenko et al. 1992; Turatto et al. 1996) over the rise time, compared against the measurements of this line velocity for SN 1986G from Phillips et al. (1987).

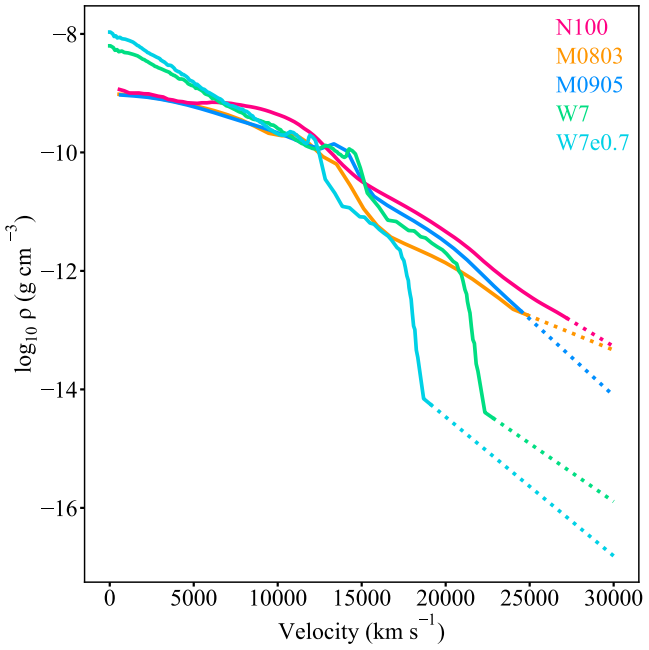

Figure 9. The density profiles of the five models discussed for SN 2021rhu expanded homologously to one day after explosion are shown as a function of velocity. These profiles arise from simulations of three different scenarios: double detonation of a sub-Chandrasekhar mass WD (orange and dark blue), delayed detonation of a Chandrasekhar mass WD (pink), and the fast deflagration of a Chandrasekhar mass WD (green and light blue). The light blue profile here is the scaled version of W7 chosen by Ashall et al. (2016) to best describe SN 1986G. The dashed regions at higher velocity are the linear extensions of the profiles in this logarithmic space with a single shell up at 30000 km s^{-1}. This extension was found to be necessary to reproduce the higher velocity ends of the calcium features.

before the *B* band peak, the material at velocities above ~ 15000 km s^{-1} is largely unconstrained by the modelling of Ashall et al. (2016) . The earlier epochs captured by the spectral sequence of SN 2021rhu gives us data with which we can constrain the faster moving ejecta and help distinguish between explosion models. It was found that material at velocities higher than the maximum velocities in the density profiles was required to fill out the bluer end of some of the features in the spectra. To this end, each of the density profiles were extended with a single shell up at 30000 km s^{-1}. The density of this shell for each profile was calculated as a linear extrapolation in logarithmic space. These density profile extensions are shown as the dotted lines in Fig 9, and their importance shall be discussed for each of the profiles in Section 4.

3.3 SN 2021rhu modelling with literature abundance profiles

The initial abundance profiles used as input to the TARDIS models are the literature abundance profiles corresponding to the four density profiles in Section 3.2: N100, M0803 M0905, and W7. The luminosity L was initially set to align the simulated spectra with the observations, the photospheric velocity $v_{\rm ph}$ chosen to match the Si II velocity, and the time since explosion set to agree with the date of first light with the inclusion of a 1d dark phase. A number of TARDIS simulations were then performed, varying these input values with the abundance and density profiles fixed, allowing us to assess the ability of these models to reproduce the observed spectral series.

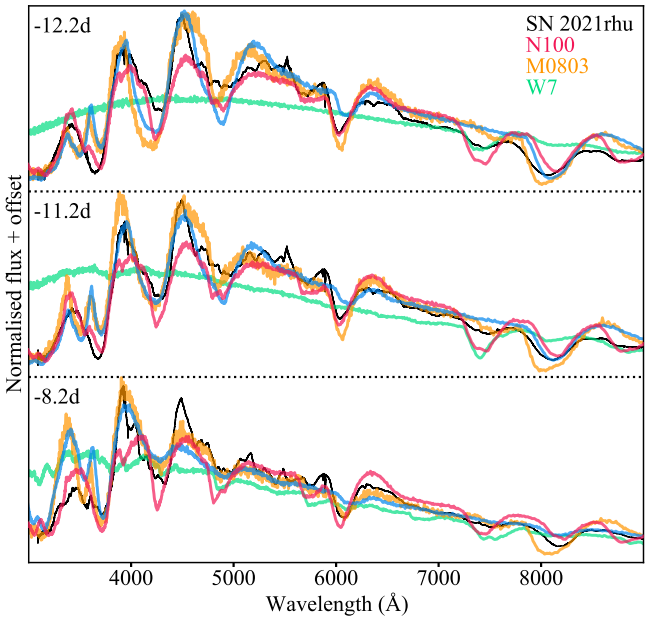

Figure 10. Best matching simulated spectra synthesised with the base literature density and abundance profiles from W7, M0803, M0905, and N100.

Figure 10 shows the results of fitting these literature abundance and density profiles ('base' models) to the three highest resolution XShooter spectra. The first synthetic spectrum resulting from the fast deflagration W7 model is featureless with the exception of the O I feature at ~ 7500Å. For a physical blackbody temperature and recreation of the observed line velocities at these pre-max phases, $v_{\rm ph}$ is required to lie above ~ 15000 km s^{-1}, and in the case of W7 this high-velocity region is only contains oxygen and neon. Some weak features begin to form in the following two epochs with the falling of the photospheric velocity, however the base W7 model is far from resembling the spectra of SN 2021rhu. The ejecta of the scaled W7e0.7 is even more compact than the W7 as visible from its density distribution in Fig 9 and would as such be even less capable of matching the observations here.

The double-detonation M0803 and M0905 models reproduce the temperature and overall shape of the earliest spectrum fairly well, with the temperature rising too quickly for the other two epochs resulting in a large flux excess in the blue. The absorption features are at roughly the correct velocities, however with strengths that do not resemble the features in the observed spectrum. The signature Si II $\lambda\lambda$6355 line, like the Ca NIR is too strong, while the model fails to reproduce the higher velocity component to the Ca H&K absorption structure. The key Ti II trough at ~ 4300Å is far too strong in the earliest epoch, owing to the large amounts of titanium that is synthesised in these double-detonation models, with this feature weakening in the later spectra due to the previously mentioned rising temperatures.

While the N100 literature model cannot reproduce the observed spectra entirely, it is the closest of the base models to doing so. With the overall spectral shape replicated for all three epochs, the temperature evolution resembles SN 2021rhu. However, like the double-detonation models, the feature strengths are a source of discrepancy in this model. Similarly to the double-detonation models, the delayed detonation N100 is incapable of filling out the higher velocity end of the Ca H&K absorption complex. There is also an over absorption in the region of the Ti II feature but in the case of N100, this stems from the large amounts of magnesium, which also produces an absorption line in this region. Finally, the N100 has an overabundance of Si when compared to SN 2021rhu. This can be seen not only in the excess absorption at ~ 4900Å, but also in the gradually growing P-Cygni emission from the $\lambda\lambda$6355Å feature across the three epochs. The velocity of this synthesised silicon feature shows very little evolution across the spectra, despite the receding $v_{\rm ph}$, once again pointing towards a larger than required silicon abundance above the photosphere.

In summary, while the delayed detonation (N100) and double-detonation models (M0803 and M0905) provide reasonably similar spectra to those observed in SN 2021rhu pre-maximum, the line strengths and in particular the lower levels of high-velocity material in the models and a mismatch in the Ti II absorption suggest that using custom abundance profiles may help provide closer matches to the data.

3.4 Custom abundance profiles for SN 2021rhu

As evident from Fig. 10, none of the tested base literature models are capable of replicating the spectra evolution we observe for SN 2021rhu. As such we require custom abundance profiles, derived through abundance tomography (Stehle et al. 2005). This technique is used to develop a custom abundance profile for an assumed density profile. Firstly, the abundances of the higher velocity material is constrained manually to match the features and shape of the earliest spectrum. Each successive spectrum has a slightly lower photosphere and therefore, constrains a new lower velocity region of the ejecta. This is performed for as many of the spectra possible until the approximations made by TARDIS become unfeasible to continue. Firstly, we derived a custom abundance profiles for the N100 model because of its closest base model match to SN 2021rhu (Fig. 10). We then used a 'projection' or scaling method (described in Section 3.4.1) to obtain models based on the other density profiles.

To distinguish the derived custom abundance profiles with the literature density profiles from the full models from the literature we use a * notation, e.g. the original delayed-detonation N100 model from the literature is referred to as N100, whereas the model with the custom abundance profile that borrows the N100 density profile is denoted N100*. This same convention is used for W7*, W7e0.7*, M0803* and M0905*.

3.4.1 Projection to other density profiles

It is clear from Fig. 9 that the N100 density profile is very similar to those of the double-detonation models, M0803 and M0905 in the regions covered by our TARDIS modelling (>11000 km s^{-1}). Therefore, instead of performing abundance tomography for each of the double-detonation models, we use the following scaling or 'projection' of the N100* onto the base M0803 and M0905 density profiles to obtain M0803* and M0905* custom abundance profiles for each species, X, given by

$$A_{\rm X,\,p^*} = \frac{A_{\rm X,\,N100^*} \times \rho_{\rm N100}}{\rho_{\rm p}} \quad (4)$$

where $A_{\rm X,\,p^*}$ refers to the new abundance profile of X from the literature model, p, and $\rho_{\rm p}$ is the density profile for each p. For example, the scaled abundance profile for Si for the M0803* model ($A_{\rm Si,M0803*}$) is calculated as the product of the abundance profile of Si in N100* ($A_{\rm Si,N100*}$) and the ratio of the density profiles of the N100 to M0803 models (ρ_{N100}/ρ_{M0803}). In each of these adjusted

models, carbon is then used as a 'filler species' to normalise the total mass fraction. The spectral evolution can then once again be calculated with TARDIS for these new models, retaining all the other input parameters from the N100* model.

Compared to the density profiles from the double detonation models, the W7 and the lower energy W7e0.7 model density profiles differ more significantly from that of the N100 in the region above 22000 km s^{-1} for W7 and 17000 km s^{-1} for W7e0.7. These large differences in the outer regions will be reflected in the synthetic spectra generated by the projected models W7* and W7e0.7*, namely their ability to reproduce the high velocity features.

This method allows us to project between similar density profiles as the variations in ejecta conditions are minimal. This can in fact be expanded to the more of the HESMA delayed detonation models (Seitenzahl et al. 2013), and double detonation models (Gronow et al. 2021), for which the scatter between the density profiles of models arising from the same explosion mechanism is similar to the scatter between the two mechanisms, making the density profiles degenerate.

3.4.2 *Modelling the host extinction corrected spectra*

As detailed in Section 2.2, the host component to the extinction correction was not included for the formation of the N100* model. Here we have recalibrated the observed spectra to account for this host extinction of $A_V = 0.42$ mag. In terms of changes to the TARDIS input parameters, the main difference will be an increase in the required luminosity as each of the observed spectra are now brighter. Similar to the projection of the N100* model to the other density profiles, we perform a similar type of projection to create an initial pass model for the reproduction of the host extinction corrected spectral series.

When we increase the luminosity input for a synthesised spectrum, this principally causes an increase in the temperature of the plasma. This in turn affects the ionisation balances of each of the species and as a result, reshapes the features in the final spectrum. In the spectra of SNe Ia, the largest contributors to the spectral features are the singly ionised species; being responsible for key structures such as the signature Si II, the 'w' shaped S II, Ca II H&K, and of course the Ti II trough. A similar effect occurs accompanies the shifting of the t parameter for time since explosion. To this end we perform a projection not to simply retain the overall species densities, but specifically the singly ionised species densities. This can be achieved by identifying the required luminosity and time at each of the epochs to match the brightness and temperature of the host extincted spectra, and then running these simulations with the raw N100* model to extract the relative fraction of singly ionised material for each species. The projection for each species X is then calculated between the initial luminosity L_0 and L with singly ionised mass fractions f using the following

$$A_{X,\,L,\,t} = \frac{A_{X,\,L_0,\,t_0} \times f_{X^+,\,L_0,\,t_0}}{f_{X^+,\,L,\,t}} \tag{5}$$

Once again for the example of silicon, the resulting Si abundance profile at the new luminosity L, and time t ($A_{Si,\,L,\,t}$), is the product of the Si abundance profile with the original parameters ($A_{Si,\,L_0,\,t_0}$) and the ratio of the relative fraction of singly ionised silicon with the original parameters ($f_{Si^+,\,L_0,\,t_0}$) with the fraction of singly ionised silicon with the new parameters ($f_{Si^+,\,L,\,t}$).

We refer to this model for the host extinction corrected observations as N100*h. The resulting synthesised spectra and analysis of this model can be seen in Section. 3.4.2.

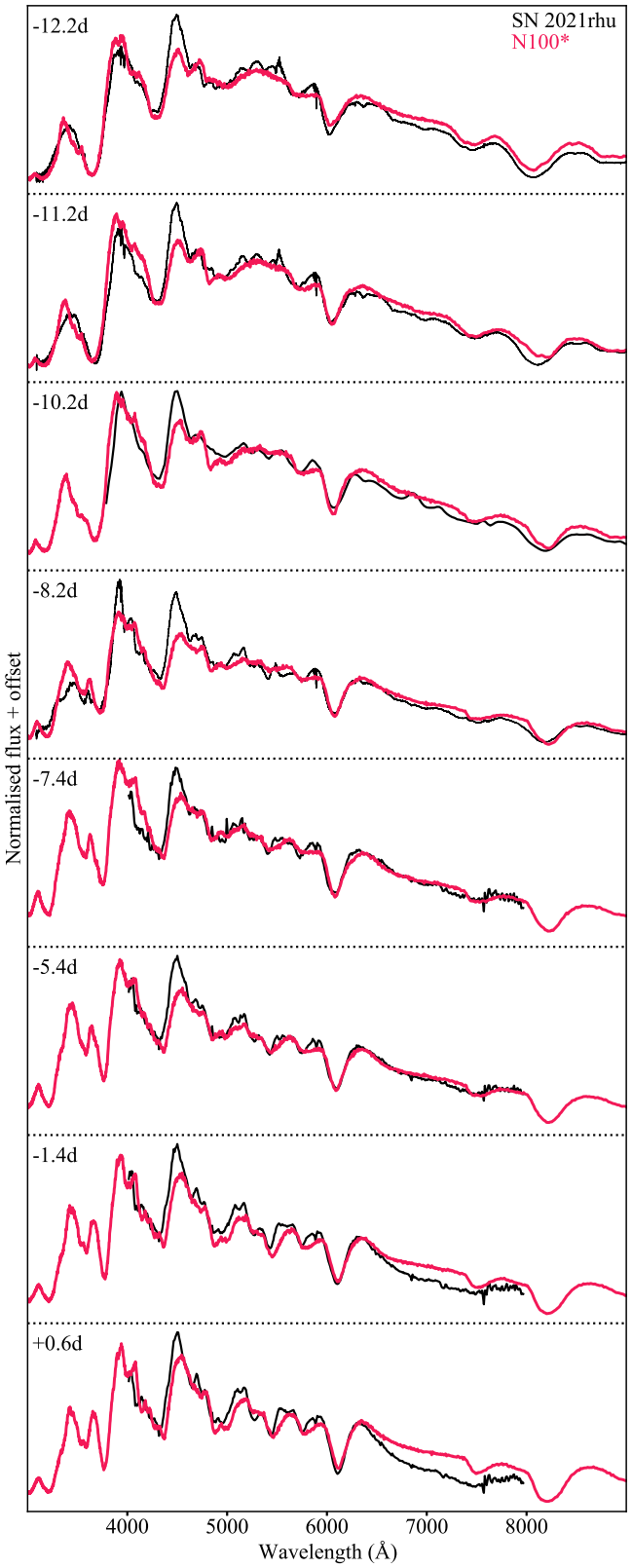

Figure 11. TARDIS simulations for the 8 spectra up to peak light with the fixed N100 density profile and custom abundance profile derived manually through abundance tomography (N100*). N100* is displayed in pink overplotted upon the photometrically calibrated spectra in black.

Table 1. TARDIS simulation parameters for the N100* and N100*h models. The * symbols denote that while the density profiles correspond to the literature N100 model, the abundance profiles are custom built for SN 2021rhu. N100*h is the model designed for the host extinction corrected spectra (see Section 4.5).

Phase	t (d)		v_{ph} (km s^{-1})		L (log L$_\odot$)		T_{BB} (K)	
	N100*	N100*h	N100*	N100*h	N100*	N100*h	N100*	N100*h
-12.2	6.0	6.5	16000	16000	8.38	8.56	7378	7788
-11.2	7.0	7.5	14500	14500	8.53	8.71	8103	8622
-10.2	8.0	8.5	14000	14000	8.68	8.88	8413	9177
-8.2	10.0	10.5	13500	13500	8.93	9.13	8712	9555
-7.4	10.8	11.3	13200	13200	9.04	9.24	9058	9988
-5.4	12.82	13.32	12700	12700	9.19	9.39	9216	10218
-1.4	16.78	17.28	11500	11500	9.31	9.53?	9193	10242
+0.6	18.79	19.29	11300	11300	9.34	9.57?	8823	9819

4 RESULTS

In this section, we discuss the results of our modelling efforts and the link to the explosion models. A key feature of the spectra of transitional events like SN 1986G and SN 2021rhu is the strong titanium absorption in the blue ~4300 Å. As discussed in Section 1, there is an open question of whether the presence of titanium absorption in these SNe is due to an increase in titanium abundance (that can be linked to explosion mechanism) or it is a temperature effect, where lower temperatures in these sub-luminous events produce conditions where titanium absorption is more pronounced. In Section 4.1 we detail the fiducial custom model N100* with the delayed detonation density profile. In Section 4.2 we describe the results of the modelling using the W7* models, and in Section 4.3 we highlight the results of the two custom abundance profiles with the double-detonation density profiles. Finally, we present the results of the N100*h model for the host extinction corrected spectra in Section 4.5.

4.1 N100* - delayed detonation density profile

The delayed-detonation N100 model is a characterized by the highest densities in the outer layers of any of the models considered here (see Fig. 9). The abundances of the original N100 model as function of velocity were presented in Seitenzahl et al. (2013). As discussed in Section 3.4, we have derived new fully custom abundances using the abundance tomography technique (e.g. sequential fitting of multiple epochs) with the N100 density profile to produce a best-matching model (N100*) to the data.

With the fixed N100 density profile, the requested luminosity tuned to the brightness of each spectrum, and v_{ph} roughly following the velocity of the Si II $\lambda\lambda$6355Å line (Tanaka et al. 2008), only free parameter to tune the temperature to match the overall spectral shape is the time since explosion. From the fitting of the light-curve rise (see Section 2.3) we know the first spectrum to be 5.18 ± 0.25 d after first light. Converting this to time since explosion then requires the inclusion of some dark phase to allow for the photons to escape the ejecta. As mentioned in Section 2.3, the power law index of this fit can be taken as a proxy for dark phase, and with an index close to the average value we can assume a dark phase up to a couple of days. The best matching spectral shape was found to occur with the first spectrum of SN 2021rhu assumed to be at 6 days past explosion, which implies a dark phase of 0.58±0.78d. This time since explosion is therefore in agreement with the fit to the early light-curve rise. The synthesised spectra with the N100* model can be seen in Fig. 11 over optical wavelengths and Fig. 12 for the three epochs of infrared coverage with the XShooter spectra. The derived abundance profile can be seen in Fig. 15. The best-matching TARDIS parameters for the models for each spectral epoch are listed in Table 1.

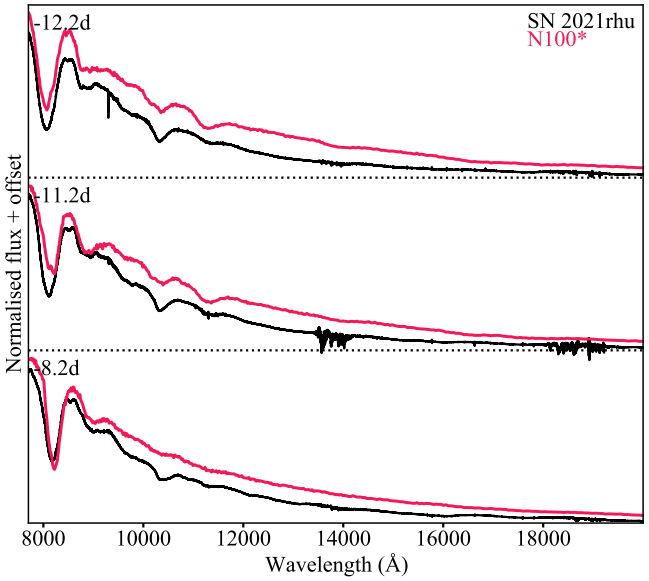

Figure 12. TARDIS simulations for the 3 XShooter epochs in the infrared fixed N100 density profile and custom abundance profile derived manually through abundance tomography (N100*). N100* is displayed in pink overplotted upon the photometrically calibrated spectra in black.

4.1.1 −12.2d

The top observed spectrum of Fig. 11 was recorded 12.2 d before maximum light with the XShooter spectrograph. Oxygen was initially used as a filler species to fill out the remaining mass fraction in the model, however this caused a strong over-absorption of the O I feature to the blue of the Ca NIR at ~7500Å. It was found that in order to reproduce the strength of this feature accurately we needed as little as a 3% oxygen mass fraction in the outer ejecta. We instead turned to carbon as the filler species. While this allows the model to reproduce all the feature strengths accurately, this now leaves the N100* model with a mass fraction of carbon in these outer regions of 90%. This will be addressed in Section 4.4.

In order to fill out the full velocity extent of the Ca H&K feature, it was necessary to extend the N100 density profile upwards with an additional shell at 30000 km s^{-1}(see Fig. 9). The calcium in this shell made up 1 per cent by mass with 69 per cent oxygen and 30

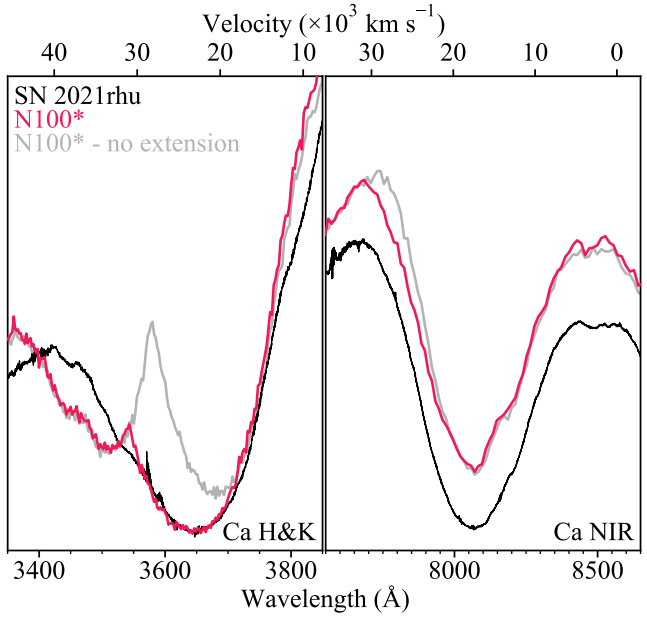

Figure 13. Zoomed view of the Ca H&K and NIR features comparing the observed -12.2d day spectrum of SN 2021rhu (black) against the synthesised spectra from N100* with (pink) and without (purple) the density profile extension up to 30000km s^{-1}. The extended shell has a calcium mass fraction of 1%.

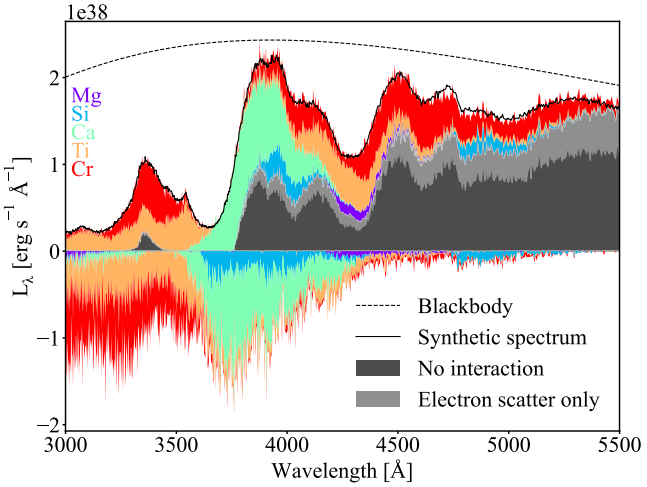

Figure 14. Spectral energy decomposition plot of the -12.2d synthetic spectrum from the N100* model showing the contributions of different species to the signature Ti II feature. Shaded regions above zero flux represent emission with absorption shown below. The dotted line represents the initial emitted blackbody and the synthetic spectrum is overplotted in black.

per cent carbon. A comparison of the synthesised spectrum, at this earliest epoch, with and without this density extension can be seen in Fig. 13. The shoulder contamination in the blue of the Ca H&K is produced by titanium and chromium and does not appear in the observed spectra until the −8.2d spectrum. The wavelength range of the −10.2d spectrum does not cover this feature and it is therefore unclear if this neighbouring feature is present at this epoch. Reducing the relative abundances of titanium and chromium can remove this feature however at great cost to the reproduction of the key feature of interest at ∼4300 Å.

As evident from the spectral energy decomposition of the synthetic −12.2d spectrum in Fig. 14 in the 3000 –5500 Å, the so-labelled Ti II feature is in fact formed by a delicate balance of a few different species. While magnesium does typically show fairly strong absorption in this region, it was found that the evolution of the feature could be closely replicated without this contribution - as such only trace amounts of magnesium are present in N100*. The peak at ∼ 4500Å is under luminous in the synthetic spectrum compared to the observed data, a discrepancy which in fact remains throughout the epochs modelled. The largest contributor to this peak is seen to be chromium, meaning that an increase in chromium could boost this flux. It is clear however that the chromium abundance greatly affects the spectral shape in the surrounding regions which match the observed data closely, and therefore, is well constrained.

While noted that there exists an overall flux excess into the infrared for the calculations, Fig 12 shows a comparison between the synthesised spectra and the XShooter epochs in this region. The prominent feature in the blue end of this region is the Ca NIR, with the feature to the red of this being predominately formed by magnesium. The strong feature to the red of this is also expected to be formed by magnesium however in the synthesised spectrum is in fact produced as a double feature with magnesium and the large carbon content as the filler species.

4.1.2 -11.2d

The second XShooter spectrum was observed just a day after the first, at a phase of -11.2d before maximum light. The shape of the spectrum is very similar to the first epoch but has higher luminosity and slightly slower velocities. Similar to the first spectrum, there exists a blue shoulder to the Ca H&K which is absent in the observed spectrum, as well as an underproduction of the luminosity of the ∼ 4500Å peak. Between the first and second epoch we require a large rise in the titanium mass fraction from 0.002% to over 1% along with a slight boost in chromium from 0.01% to ∼0.04%. It was also found that the carbon mass had to be dropped completely between the first and second photosphere as to avoid forming the C II **6580**Å line in the later spectra towards peak. This was instead replaced with oxygen. Due to 99% of the oxygen in this region being mostly in the singly ionised state at this epoch, this does not affect the strength of the well matched O I feature around 7500Å. This ionisation balance will gradually sway towards neutral oxygen with successive epochs and causes a boost to this feature in the final 2 spectra (-1.4d and +0.6d). This reduction of carbon does not visibly reduce the contribution to the feature just above 10000Å in the infrared spectrum at this epoch.

4.1.3 -10.2d

The -10.2d spectrum was obtained with the P60+SEDM, which has lower spectral resolution and smaller wavelength range than XShooter and it does not cover the the Ca H&K feature. Therefore it is unclear at which point between -11.2d and -8.2d the double peaked nature of this feature appears. At this epoch the best-matching model spectrum (parameters in Table 1) exhibits excess Si II absorption at ∼ 5000Å. This is accompanied by the enhanced absorption in the principal Si II $\lambda\lambda$6355 feature. With the photospheres of the second and third epochs only separated by 500km s^{-1}we are fairly limited in our freedom to alter the silicon abundance.

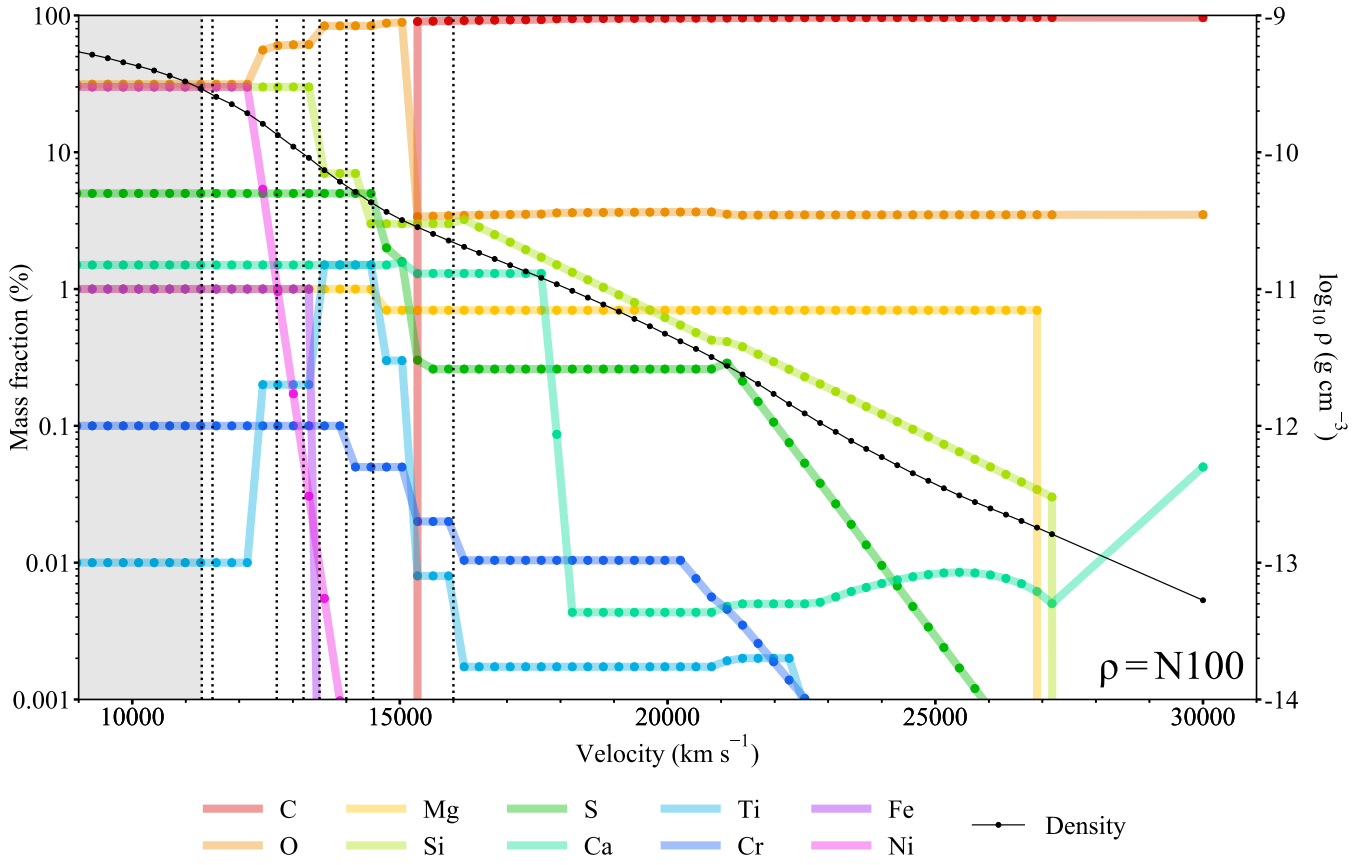

Figure 15. *Top:* The derived N100* abundance profile for SN 2021rhu. The circles represent the shells and the vertical dotted lines indicate the photospheric velocities for each of the synthesised spectra. The shaded region indicates the ejected material below the final photosphere; this material is not present in any of the simulations and therefore is not constrained in the model. It should be noted here that the photospheric velocities do not necessarily align exactly with the discrete shell velocities and as such the first shell in the model is taken as the first shell at this v_{ph} or above. The N100 density profile is also overlayed in black. *Bottom:* The raw N100 model from the literature displayed for visual comparison.

4.1.4 -8.2d

The -8.2d spectrum is the first point in which we stray from a one-day cadence, and also the final epoch for which we have an XShooter spectrum. The v_{ph} has dropped by 500 km s^{-1}with an increased luminosity and temperature compared to the previous epoch. The shoulder feature to the Ca H&K starts to show through in the data here. While the model matches the velocities very well, as well as the Ca II absorption, there is a slight boost to the flux in the Ti/Cr shoulder along with the neighbouring peak to the blue. This is likely to be the result of a temperature that is too high, however raising the photosphere to reduce the temperature would disrupt the other well matching features. As discussed in Section 3.1, the photospheric approximation made by Tardis can cause such issues as a single photospheric velocity is assumed across the spectrum instead of it varying with wavelength; this therefore may be the cause behind this slight boost in flux.

With the carbon drop off introduced above the -11.2d photosphere, the contribution of carbon to the magnesium feature in the infrared has faded completely, leaving a trace feature produced by the remaining magnesium in the model.

4.1.5 -7.4d and -5.4 d

From the -7.4d spectrum onwards we have only spectra coming from the SPRAT instrument on the LT, which while retaining a fairly high spectral resolution brings a significant reduction in wavelength coverage (rest frame ~ 4000 – 8000Å). Therefore, the spectra miss the Ca H&K and the neighbouring peaks in the blue end, and the Ca NIR triplet in the red. The remaining features in between however are shown to be reproduced well in the remaining few simulations. As previously seen, the photospheric velocity continues to decrease while the luminosity and temperature increase for both these spectra. For an accurate reproduction of the spectral shape for the remaining epochs - most importantly for the -7.4d and -5.4d spectra - iron is required in the ejecta. In the N100* model the iron in the ejected material extends out to 13000km s^{-1}, making up 1% of the mass in each of those shells.

4.1.6 -1.4d

The -1.4 d epoch is the first epoch for which a direct comparison can be made between our N100* model and the model produced by Ashall et al. (2016) for SN 1986G. The N100* spectrum was synthesised with v_{ph} = 11500km s^{-1}, a luminosity of 7.81×10^{42}erg s^{-1} and a converged blackbody temperature of 9193K. The preferred

SN 1986G model with the W7e0.7 density profile at the -1d epoch required v_{ph} = 8800km s^{-1}, a luminosity of 3.98×10^{42}erg s^{-1} and a blackbody temperature of 9500K. As these two models are built upon different density profiles, the photospheric velocity is expected to be different; the N100 density profile is higher in the region ~ 6500−13000 and as such the material is more optically thick making for a higher photospheric boundary. This can also explain the temperature difference. The lower luminosity is to be expected too as SN 1986G is sub-luminous in comparison to SN 2021rhu. A large increase in nickel and iron was required for the modelling of the final two spectra of SN 2021rhu, with the mass fractions increasing to 30% for nickel and 1% for iron. As trace amounts of iron group material was required in the ejected material above this 11500km s^{-1}photosphere, the need for a fairly compact nickel distribution is well constrained.

4.1.7 +0.6d

Once again, the +0.6d epoch lines up nicely in time with a reference spectrum for SN 1986G taken at +1d. The N100* photosphere is placed at v_{ph} = 11300km s^{-1}, with a luminosity of 8.37×10^{42}erg s^{-1} and a converged blackbody temperature of 8823K, marking the first point in which the temperature of the blackbody has decreased in the synthetic spectral series. For the SN 1986G model the input parameters were v_{ph} = 7800km s^{-1}and a luminosity of 4.37×10^{42}erg s^{-1} making for a blackbody temperature of 9700K. Due to the large proportion of radioactive nickel in the ejecta, and the 5 day time jump that would be required, the modelling of the +5.6 day spectrum is unfeasible with Tardis and as such we cease the photospheric modelling here. There are nebular spectra available for SN 2021rhu however as of yet Tardis does not have nebular modelling capabilities and as such the modelling of these is outside the scope of this work.

4.1.8 Summary of delayed detonation N100 comparison*

The N100* model recreates the observed spectral series of SN 2021rhu in terms of spectral shape, feature strengths, and line velocities. There of course exist a number of discrepancies between the synthesised spectra and the observations. The main differences include the consistent underproduction in the peak at ~4500 Å throughout the evolution up until the final spectrum taken at just after peak, and the contamination of titanium and chromium to the blue wing of the Ca H&K in the earliest two epochs. The Tardis parameters used for each of these simulations as well as the resulting blackbody temperatures can be found in Table 1.

Figure 15 provides a side by side comparison of N100* with the namesake delayed detonation model N100 from the literature. We note here that the somewhat step-like nature of the custom model is an artefact of the abundance tomography process as the compositions between the photospheres were, for the most part, kept uniform with velocity. As evident from Fig 15 the N100* strays from the N100 in many ways. Firstly the shell extension up to 30000 km s^{-1}does not exist in the base model, with the calcium abundance tapering off below 0.001% around 20000 km s^{-1}. While the N100* titanium and chromium follow the rough velocity distribution found in N100, we require significantly enhanced mass fractions of titanium to produce the evolution of the titanium trough. The iron and nickel content of N100* is more compact than N100 and is fairly well constrained as these elevated levels were required for the final two spectral epochs however caused disagreement with the data when introduced at higher velocities. Finally the extreme carbon abundance found in N100* through its use as the filler species indicates that we require much less material in these outer regions. This will further be explored in Section 4.4

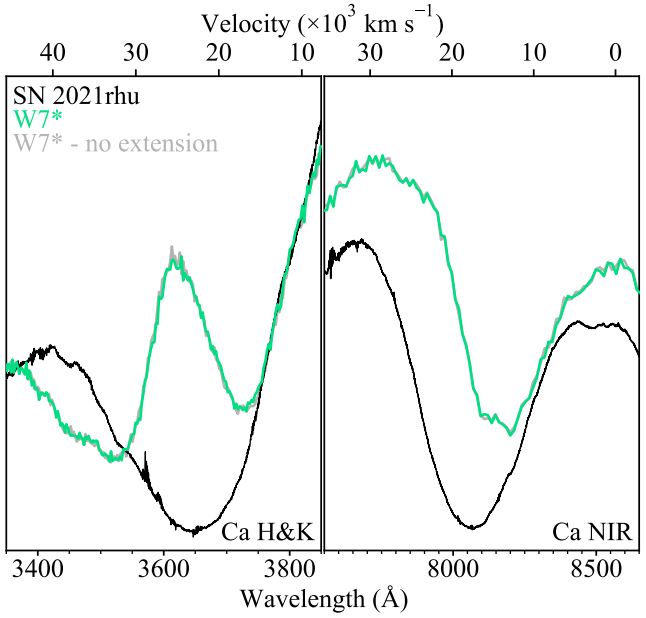

Figure 16. Zoomed view of the Ca H&K and NIR features comparing the observed -12.2d day spectrum of SN 2021rhu (black) against the synthesised spectra from W7* with (green) and without (purple) the density profile extension up to 30000km s^{-1}. The extended shell has a calcium mass fraction of 100%. While there is an increase in absorption due to this additional calcium, it is not enough to reconcile the simulation with the observed spectrum.

4.2 W7* - deflagration density profile

Here we show the results of the projection of the N100* model to the W7 density profile to create W7*. The resulting synthesised spectra for W7*, along with the double-detonation models, M0803* and M0905*, are presented in Fig. 17. In Fig. 9, it can be seen that above the threshold of ~ 15000 km s^{-1}explored in the modelling of SN 1986G, the density profiles of the deflagration models, W7 and W7e0.7 are significantly lower than the delayed-detonation (N100) and double detonation (M0803, M0905) profiles and show a sharp drop off in density.

Figure 16 shows the impact of these low densities in the outer ejecta (not probed by SN 1986G spectra) on the Ca II H&K and Ca II NIR triplet features in the earliest −12.2 d spectrum of SN 2021rhu. The W7* model is found to be a bad match to the observed data because it fails to match the high-velocity material and as a result the raw W7 density profile is insufficient in the context of the early evolution. The lower energy W7e0.7 density profile is more compact than the raw W7 density profile and, therefore, has even lower densities in these outer regions. We, therefore, also rule out the favoured density profile (W7e0.7) for SN 1986G as a candidate model for SN 2021rhu. As discussed in Section 3.2, we also extended the density profile of the W7* model with a shell at 30000 km s^{-1}to see if this provides a better match to the data. Even filling this extension shell to be 100% Ca only strengthens the synthesised feature slightly and still greatly underproduces the feature when compared to the observed spectrum. From

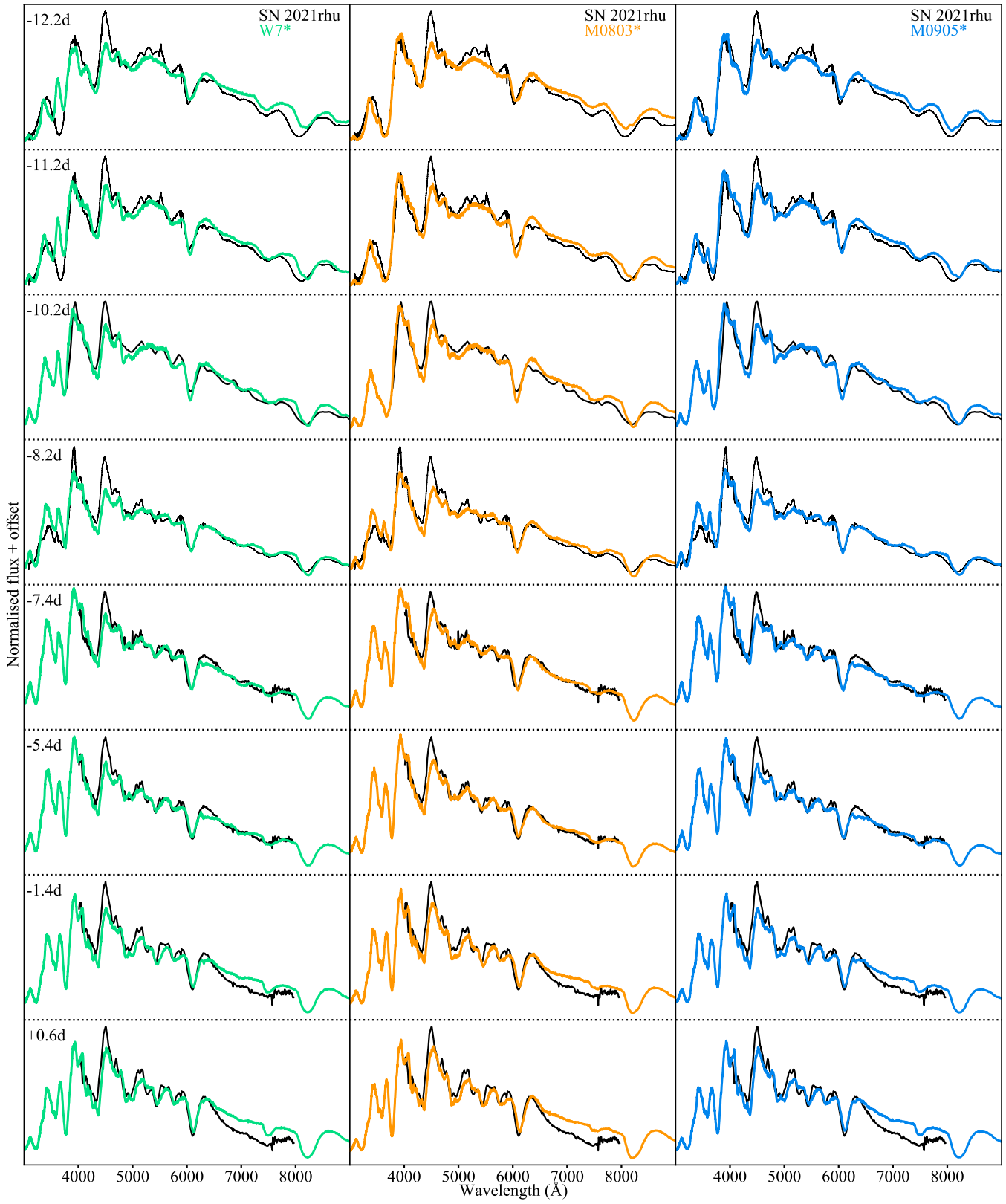

Figure 17. The synthesised spectral sequence produced from the models obtained through the projection of the N100* to the W7, M0803, and M0905 density profiles.

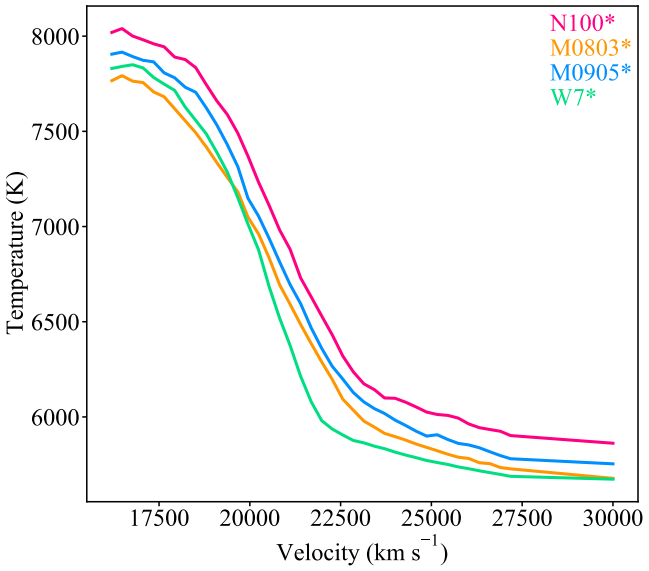

Figure 18. The temperature profiles for the -12.2d spectrum synthesised with the N100* model and then the models formed by the abundance profile projection. As expected, the different density profiles result in difference temperature profiles and in turn have an impact on the species ionisation states and feature formation, however these effects are negligible and within the proposed uncertainties of the model.

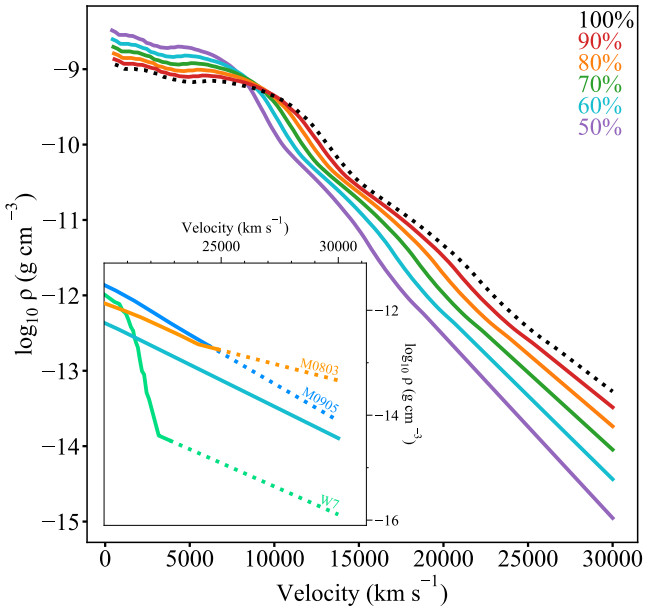

Figure 19. The result of the energy scaling upon the N100 density profile. The profiles with lower kinetic energy are less able to accelerate the ejected material to high velocities and therefore possess a more compact ejecta structure. The black dotted line represents the base N100 density profile with the 30000 km s^{-1}extension. The inset displays the location of the high velocity tail of the preferred 60% scaled density profile between the W7 and double detonation profiles.

this we can also conclude that the extended W7 density profile is not feasible for this object. When comparing to the literature W7 model, the only species present in the ejecta above ~ 14000 km s^{-1}are neon and carbon, meaning that even if the density extension was sufficient for the higher velocity material, the required abundance profile would differ greatly from the deflagration prediction in the literature.

4.3 M0803* & M0905* - double detonation density profiles

In this section, we aim to compare the observed spectra of SN 2021rhu to those of the projected models with the double detonation density profiles, M0803* and M0905*. We note that the density profiles used in this projection are those with the linear extrapolation in log space up to 30000 km s^{-1}as discussed in Section 3.2.

The synthesised spectra for these models can be seen in Fig 17 and are found to reproduce the observed data well. There are a few differences and discrepancies that arise as a consequence of the radiative transfer effects caused by the density profile switch. However, we consider these to be negligible as the required changes to the abundance profiles would be of a similar order as the uncertainties on the abundances proposed as 25%.

Figure 18 shows the difference in the resulting temperature profiles between the four different models with same input parameters for the −12.2d epoch. The temperature profiles are found to be in good agreement with differences of <10% between the most extreme models (W7* and N100*). Here we reiterate that it is not the temperature difference that rules out W7*, but the insufficiently low densities in the high velocity regions.

4.4 N100_60* - reducing the carbon

As outlined in Section 4.1, through the use of carbon as the filler species in the derivation of the N100* model, the resulting profile is comprised of ~ 90% carbon by mass fraction in the region above ~ 15000 km s^{-1}. With the M0803 and M0905 density profiles being slightly smaller in this higher velocity regime than the N100, the projected models M0803* and M0905* contained slightly lower carbon abundances in the region of 80-90%.

While we are able to constrain the velocity extent of the unburnt carbon, as such a presence of carbon deeper into the ejecta causes discrepancies between the synthesised spectra and the observations towards peak, we are unable to put solid constraint upon the abundance of carbon in these outer regions. As such the aim is to be able to reduce this carbon abundance to equal the oxygen abundance. To this end, we turn to the kinetic energy scaling formulation in Equations 2 and 3. A lower kinetic energy version of the N100 density profile would have smaller densities in this higher velocity region and therefore the abundance profile would need less padding in this regime.

Figure 19 shows the resulting density profiles when scaling the kinetic energy by a range of different fractions. Reducing this energy to 60% was found to be sufficient to bring the carbon mass fraction to similar magnitudes as seen for the oxygen. The N100* model was projected onto this scaled density profile as was performed before for the M0803*, M0905*, and W7* models. The inset of Fig 19 displays the location of this preferred 60% profile in the context of the other literature density profiles. Required to be lower in density than the M0803 and M0905 density profiles as the M0803* and M0905* also possess massive amounts of carbon, this profile is also required to possess higher densities than the W7 profile in this high velocity regime as to be able to produce the high velocity edges of the calcium features.

This reduced carbon model with the scaled density profile is la-

belled as N100_60*, and the resulting synthetic spectral series can be seen in Fig 20.

4.5 N100*h - corrected for host extinction

A model to reproduce the higher luminosity observed spectral series in which we corrected for host extinction was produced through the projection method described in Section 3.4.2. The rising luminosities of the simulations bring with them rising temperatures and it is found that the 60% kinetic energy scaling of the N100 density profile used for the N100_60* model has insufficiently low densities in the region around 12000 km $s^{-1}$to faithfully reproduce the later spectra. As such the projection is calculated from the base N100* model. Due to the sizeable increase of the IME abundances in the outer regions, the filler carbon content of the outer ejecta is greatly reduced from N100* to be in line with the oxygen abundance. This model for the host extinction corrected observations is labelled as N100*h. A push back in time since explosion of 0.5 days was also found to be required to roughly match up the small peak at ~3500Å in the first two epochs.

The synthesised spectra can be seen in Fig 4.5, and once again this projection is able to well reproduce the observed data. As before, we argue that any modifications that would be required to tweak the model to match the data as well as N100*, are within the estimated uncertainties of the abundances.

This projection however does have two key drawbacks. Firstly it is built upon the assumption that the first ionisation state of each species is the only ion contributing to the final spectrum, the other ions are left unconstrained in this projection. While these are not the only contributing ions, they are the most important and are therefore required to be kept as constant as possible. The second drawback to this method is that the single ion mass fraction for the new luminosity L ($f_{X^+, L, t}$) is measured from the initial N100* model, and the very nature of changing the abundance balance will impact the state of the plasma and the ion balance of each species. This could be overcome by iterating the process two or three times to draw closer to keeping the ion density constant between N100* and the host extinction model, however we chose to make the small tweaks by hand. Once again carbon and oxygen were employed as normalisation species.

5 DISCUSSION

For SN 2021rhu we developed the base N100* before projecting it to the M0803, M0905, and W7 density profiles. The key takeaway from this abundance profile projection is that any of these three density profiles - as well as many others that have not been presented here **need ref for this** - can provide a physically plausible description of the ejecta in SN 2021rhu. The concrete conclusion from this modelling is not the mass fraction model specific to the N100 density profile - seen in Fig. 15 - but the product of this with the N100 density profile itself. This product is seen as the numerator in Equation 4 and describes a specific density profile for each species (hereby referred to as a species density profile). As these species density profiles are independent of the underlying density profile, they can be compared against models from the literature.

5.1 Comparison to literature models

The source chosen for these model comparisons is the Heidelberg Supernova Model Archive (HESMA), which is of course the source of the N100, M0803, and M0905 raw models. In Fig. 22 we see

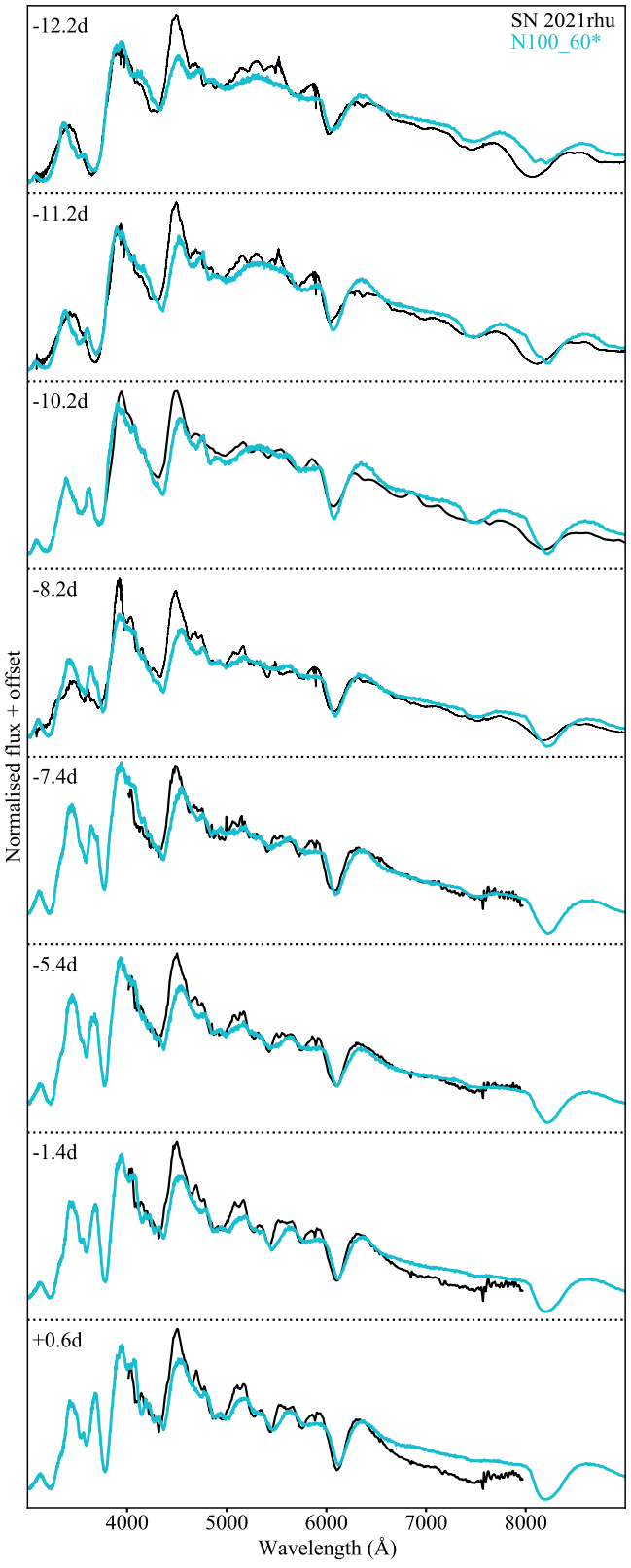

Figure 20. TARDIS simulations for the 8 spectra up to peak light for the reduced carbon model N100_60* calculated as the projection of N100* onto the 60% kinetic energy scaled N100 density profile.

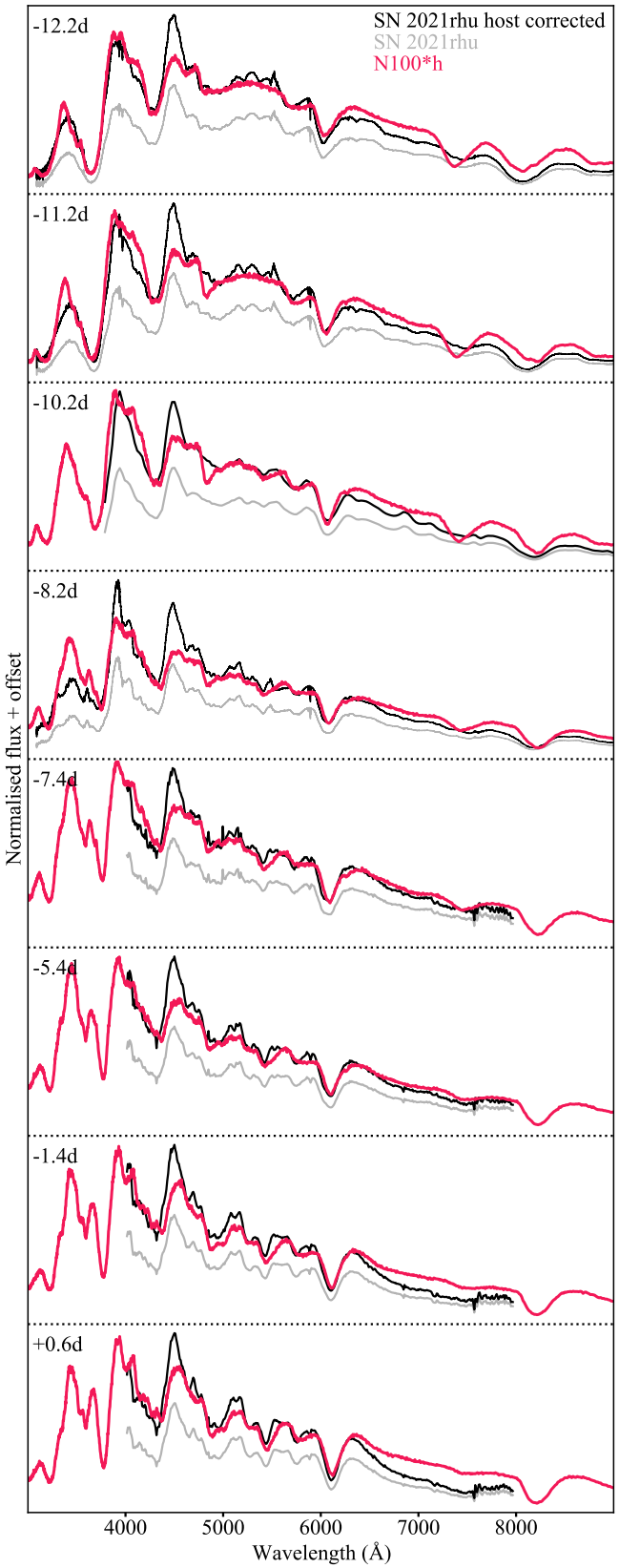

Figure 21. TARDIS simulations for the 8 spectra up to peak light for the model to the host extinction corrected observations N100*h. The grey spectra at each epoch are the observations seen for all the other models without the host extinction corrections and are included here to demonstrate the size of the luminosity difference.

comparisons for these species density profiles of some of the literature models against the N100* model (black dotted) and the N100*h (black solid) lines. These host extinction and no host extinction models act as limits with the species densities for SN 2021rhu lying somewhere in the shaded region between. It is noted here that although the abundance profiles differ for between N100*, M0803*, M0905*, W7* and N100_60*, the species density profiles remain constant through the density profile projection and as such the dotted lines in each panel represent all these models.

The faded coloured lines represent individual HESMA models, with the solid coloured lines as means for each set of literature models. The density profiles used for these products were taken at 1 day post explosion.

Due to its role as a normalisation species, the SN 2021rhu carbon distribution is the only species for which the species density profile changes among between all the different models. The dotted line in this panel therefore comes from the reduced carbon N100_60* model as a lower bound.

As evident from the magnesium, silicon and sulphur panels, the derived abundance profile has significantly lower abundances of these species in the outer regions than the literature models. This is to be expected for the N100* model without host extinction as the need for these lower abundances arises from a lower ionisation state within the plasma. As a subluminous Type Ia, the simulated spectra of SN 2021rhu are synthesised with lower requested luminosities than the normal luminosity counterparts. This lower luminosity makes for a lower temperature ejecta and in turn brings the ionisation state of the ejected material down. We see that when we bring up the luminosity for the N100*h model the temperature increases and the mass fraction of singly ionised material drops, meaning that more of each species overall is required to retain this amount of singly ionised material.

Moving towards the iron group elements we find a bump in the profile of titanium which was found to be required to consistently produce the trough feature in a number of spectra along the rise. This bump peaks to values in line with many of the double detonation models however these possess unreasonably high titanium abundances at higher velocities in the context of SN 2021rhu. Titanium is not the only species for which the double detonation models overpredict the abundances at higher velocities, this is in fact the case ubiquitously across the species - with the exception of carbon which as mentioned later is free in N100*. Finally looking to the heaviest species in the model, we find a more compact composition of iron and nickel in SN 2021rhu than found in either the double detonation of delayed detonation models, with it instead lying in a similar region to the merger models.

While unable to provide a strict answer upon the correct explosion mechanism, this analysis is able to rule out the double detonation scenario for this transitional event. Although the merger models produce similar distributions for iron and nickel to those seen in N100*, they greatly underproduce other key elements - namely titanium, chromium, and calcium. For the majority of the elements in the model, the delayed detonation mechanism lies between the double detonations and the merger in this parameter space which is also home to the N100*. It should be made clear that we do not conclude SN 2021rhu to have arisen from a delayed detonation scenario, merely that it provides a better description of the object than the other two mechanisms here.

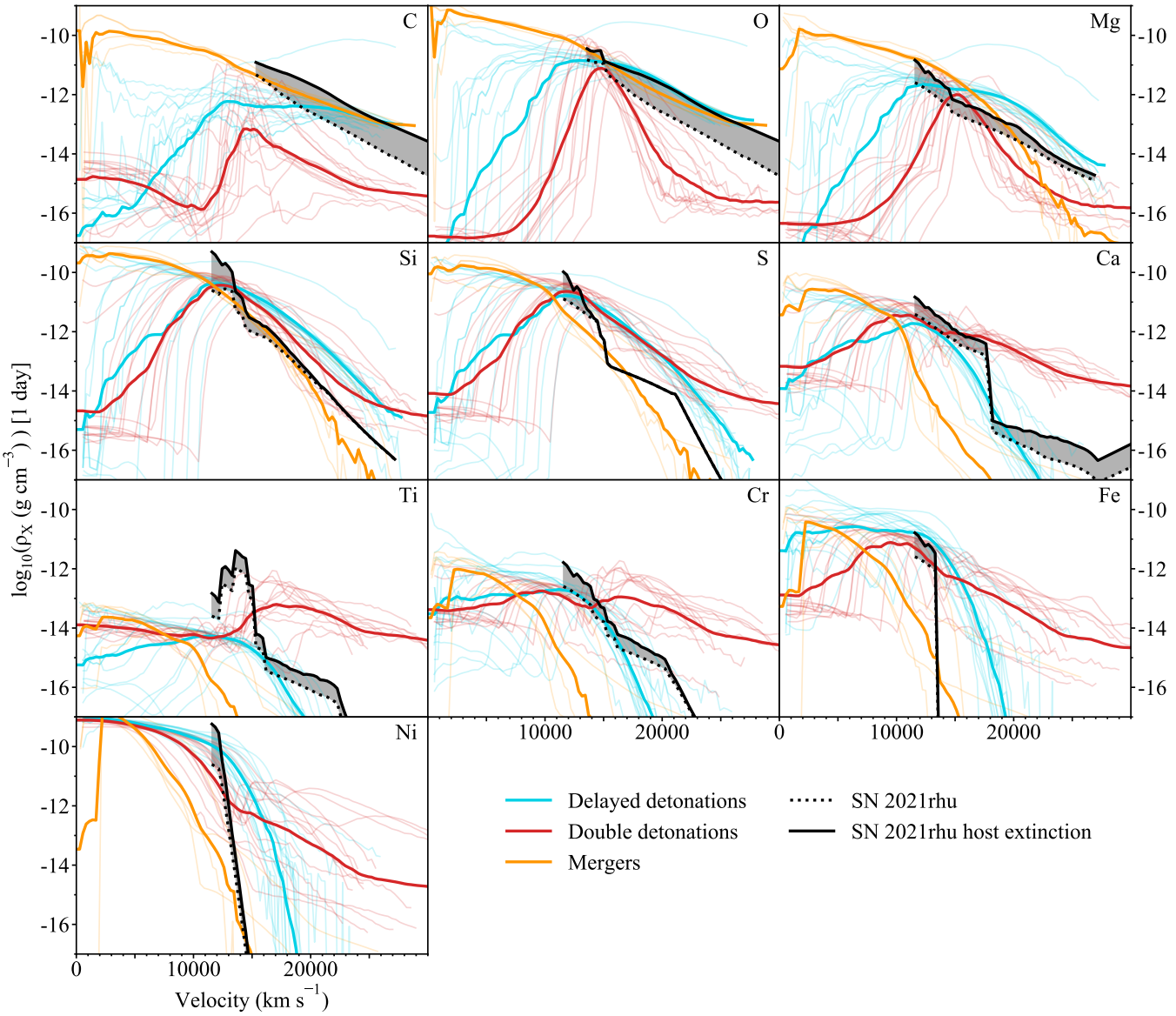

Figure 22. Comparisons of the derived species densities for SN 2021rhu without host extinction (black dotted) and with host extinction (black solid) against the double detonation (Gronow et al. 2021) (red), the delayed detonation models (Röpke et al. 2012) (blue), and the four available merger models from HESMA (Pakmor et al. 2010, 2012; Kromer et al. 2013, 2016) (orange). The thick lines are mean profiles calculated for each of the mechanisms.

6 CONCLUSION

Through abundance tomography we produced a custom abundance profile to describe the spectra evolution of SN 2021rhu using the N100 density profile. We subsequently showed that this custom model - N100* - could be projected onto other density profiles to provide an equally valid description of the data within the estimated uncertainties of the abundance profiles. This shows that many different density profiles from many different explosion mechanisms could potentially be used to produce the observed spectra, and as such this cannot be used alone to discriminate between explosion mechanisms with similar density profiles. We also demonstrated that the preferred density profile of Ashall et al. (2016) for SN 1986G (the scaled W7) has insufficient densities in the outer regions to produce the higher velocity features of SN 2021rhu in the earliest spectra. This was also the case for the normal W7 density profile.

With the large scatter on the correlation between host extinction and diffuse interstellar band strength, the amount of extinction from the host galaxy in the case of SN 2021rhu is fairly unconstrained. We took the mean measure of host extinction as an upper limit due to the fact that other similar transitional objects with this Ti II feature have all been subluminous. Through a second projection method, we produced N100*h to reproduce the host extinction corrected spectra. This projection operated under the assumption that the singly ionised intermediate mass elements were the sole contributors to the spectral features. As evident from the ability of N100*h to match the spectral evolution, this assumption is sufficient.

In order to compare the resulting models to those coming from the literature, it was required to look at the product of the abundance profile with the density profile being used, as this is what remains constant between the different models developed here. These species

density profiles were in turn compared to literature models arising from the double detonation mechanism, the delayed detonation mechanism, and the violent merger mechanism. It was clear from this comparison that neither the violent merger model, nor the double detonation model are sufficient descriptions of SN 2021rhu. For the majority of the species, SN 2021rhu appears to lie in a similar region of the parameter space to many of the delayed detonation models. This however is not the case for a couple of elements, namely magnesium and titanium which both play a role in the Ti II trough complex which differentiates SN 2021rhu from normal thermonuclear events.

ACKNOWLEDGEMENTS

This research made use of Tardis, a community-developed software package for spectral synthesis in supernovae (Kerzendorf & Sim 2014; Kerzendorf et al. 2020). The development of Tardis received support from the Google Summer of Code initiative and from ESA's Summer of Code in Space program. Tardis makes extensive use of Astropy and PyNE.

This work made use of the Heidelberg Supernova Model Archive (HESMA), https://hesma.h-its.org.

The data presented here were obtained in part with ALFOSC, which is provided by the Instituto de Astrofisica de Andalucia (IAA) under a joint agreement with the University of Copenhagen and NOT.

The image of the host galaxy NGC7814 along with SN 2021rhu was taken by the Chart32 team. Prompt 7 CTIO/UNC Chile, Chart32-Team.

REFERENCES

Ashall C., Mazzali P. A., Pian E., James P. A., 2016, MNRAS, 463, 1891
Atapin K., et al., 2021, Transient Name Server Classification Report, 2021-2286, 1
Barbary K., et al., 2016, SNCosmo: Python library for supernova cosmology (ascl:1611.017)
Barna B., Szalai T., Kromer M., Kerzendorf W. E., Vinkó J., Silverman J. M., Marion G. H., Wheeler J. C., 2017, MNRAS, 471, 4865
Blagorodnova N., et al., 2018, PASP, 130, 035003
Brown P. J., Breeveld A. A., Holland S., Kuin P., Pritchard T., 2014, Ap&SS, 354, 89
Carrasco-Davis R., et al., 2020, arXiv e-prints, p. arXiv:2008.03309
Cenko S. B., et al., 2006, PASP, 118, 1396
Cristiani S., et al., 1992, A&A, 259, 63
Dhawan S., et al., 2022, arXiv e-prints, p. arXiv:2203.04241
Ferrarese L., Mould J. R., Stetson P. B., Tonry J. L., Blakeslee J. P., Ajhar E. A., 2007, ApJ, 654, 186
Filippenko A. V., et al., 1992, AJ, 104, 1543
Firth R. E., et al., 2015, MNRAS, 446, 3895
Fitzpatrick E. L., Massa D., 2007, ApJ, 663, 320
Fouesneau M., 2022, pyphot, https://github.com/mfouesneau/pyphot
Freudling W., Romaniello M., Bramich D. M., Ballester P., Forchi V., García-Dabló C. E., Moehler S., Neeser M. J., 2013, A&A, 559, A96
Gillanders J. H., McCann M., Sim S. A., Smartt S. J., Ballance C. P., 2021, MNRAS, 506, 3560
Gillanders J. H., Smartt S. J., Sim S. A., Bauswein A., Goriely S., 2022a, arXiv e-prints, p. arXiv:2202.01786
Gillanders J. H., Smartt S. J., Sim S. A., Bauswein A., Goriely S., 2022b, arXiv e-prints, p. arXiv:2202.01786
Ginsburg A., et al., 2019, AJ, 157, 98
Gronow S., Collins C. E., Sim S. A., Röpke F. K., 2021, A&A, 649, A155
Guillochon J., Parrent J., Kelley L. Z., Margutti R., 2017, ApJ, 835, 64
Guy J., et al., 2007, A&A, 466, 11
Kerzendorf W. E., Sim S. A., 2014, MNRAS, 440, 387
Kerzendorf W., et al., 2020, tardis-sn/tardis: TARDIS v3.0.dev3459, doi:10.5281/zenodo.3893940, https://doi.org/10.5281/zenodo.3893940
Kromer M., et al., 2013, ApJ, 778, L18
Kromer M., et al., 2016, MNRAS, 459, 4428
Leibundgut B., et al., 1993, AJ, 105, 301
Magee M. R., Gillanders J. H., Maguire K., Sim S. A., Callan F. P., 2021, MNRAS,
Maguire K., Taubenberger S., Sullivan M., Mazzali P. A., 2016, MNRAS, 457, 3254
Mazzali P. A., Chugai N., Turatto M., Lucy L. B., Danziger I. J., Cappellaro E., della Valle M., Benetti S., 1997, MNRAS, 284, 151
Miller A. A., et al., 2020, ApJ, 902, 47
Modigliani A., et al., 2010, in Silva D. R., Peck A. B., Soifer B. T., eds, Society of Photo-Optical Instrumentation Engineers (SPIE) Conference Series Vol. 7737, Observatory Operations: Strategies, Processes, and Systems III. p. 773728, doi:10.1117/12.857211
Munari U., Henden A., Belligoli R., Castellani F., Cherini G., Righetti G. L., Vagnozzi A., 2013, New Astron., 20, 30
Nugent P., Phillips M., Baron E., Branch D., Hauschildt P., 1995, ApJ, 455, L147
Pakmor R., Kromer M., Röpke F. K., Sim S. A., Ruiter A. J., Hillebrandt W., 2010, Nature, 463, 61
Pakmor R., Kromer M., Taubenberger S., Sim S. A., Röpke F. K., Hillebrandt W., 2012, ApJ, 747, L10
Parrent J. T., et al., 2012, ApJ, 752, L26
Perlmutter S., et al., 1999, ApJ, 517, 565
Phillips M. M., 1993, ApJ, 413, L105
Phillips M. M., et al., 1987, PASP, 99, 592
Phillips M. M., Lira P., Suntzeff N. B., Schommer R. A., Hamuy M., Maza J., 1999, AJ, 118, 1766
Phillips M. M., et al., 2013a, ApJ, 779, 38
Phillips M. M., et al., 2013b, ApJ, 779, 38
Piascik A. S., Steele I. A., Bates S. D., Mottram C. J., Smith R. J., Barnsley R. M., Bolton B., 2014, in Ramsay S. K., McLean I. S., Takami H., eds, Society of Photo-Optical Instrumentation Engineers (SPIE) Conference Series Vol. 9147, Ground-based and Airborne Instrumentation for Astronomy V. p. 91478H, doi:10.1117/12.2055117
Potanin S. A., et al., 2020, Astronomy Letters, 46, 836
Prentice S. J., et al., 2021, MNRAS, 508, 4342
Pskovskii I. P., 1977, Soviet Ast., 21, 675
Reusch S., 2020, ztffps, doi:10.5281/zenodo.4049711
Richmond M. W., Smith H. A., 2012, , 40, 872
Riess A. G., et al., 1998, AJ, 116, 1009
Riess A. G., et al., 2021, arXiv e-prints, p. arXiv:2112.04510
Rigault M., et al., 2019, A&A, 627, A115
Röpke F. K., et al., 2012, ApJ, 750, L19
Schlegel D. J., Finkbeiner D. P., Davis M., 1998, ApJ, 500, 525
Seitenzahl I. R., et al., 2013, MNRAS, 429, 1156
Shappee B. J., Stanek K. Z., 2011, ApJ, 733, 124
Smartt S. J., et al., 2017, Nature, 551, 75
Springob C. M., Haynes M. P., Giovanelli R., Kent B. R., 2005, ApJS, 160, 149
Steele I. A., et al., 2004, in Oschmann Jacobus M. J., ed., Society of Photo-Optical Instrumentation Engineers (SPIE) Conference Series Vol. 5489, Ground-based Telescopes. pp 679–692, doi:10.1117/12.551456
Stehle M., Mazzali P. A., Hillebrandt W., 2005, Nuclear Phys. A, 758, 470
Tanaka M., et al., 2008, ApJ, 677, 448
Turatto M., Benetti S., Cappellaro E., Danziger I. J., Della Valle M., Gouiffes C., Mazzali P. A., Patat F., 1996, MNRAS, 283, 1
Vernet J., et al., 2011, A&A, 536, A105
Williamson M., Kerzendorf W., Modjaz M., 2021, ApJ, 908, 150

APPENDIX A:

This paper has been typeset from a TEX/LATEX file prepared by the author.

Table A1. Photometric data for SN 2021rhu taken with the ZTF camera on the P48 telescope, as well as the *u* and *v* data points taken with Swift. These data have not been corrected for extinction, and has been binned to a one day cadence. The uncertainties are given in the brackets after the values as multiples of 0.01 mag.

MJD	ZTF*g*	ZTF*r*	ZTF*i*	*u*	*v*
59396.4	15.73(2)	15.61(2)			
59399.4			15.24(8)		
59400.4	14.39(2)	13.8(2)			
59402.4	13.38(2)	13.21(2)	13.42(2)		
59403.4	13.14(2)	12.9(2)	13.1(2)		
59404.4	12.93(2)				
59405.4		12.59(2)	12.82(2)		
59406.4		12.59(2)			
59407.4		12.31(2)	12.71(2)		
59408.4		12.4(2)	12.72(2)		
59409.4	12.42(2)	12.33(2)			
59410.4	12.38(2)	12.32(2)			
59410.8				13.95(5)	12.37(4)
59411.4	12.39(2)	12.43(2)	12.78(2)		
59412.4	12.43(2)	12.32(2)			
59413.5				14.15(5)	12.38(4)
59414.4	12.49(2)	12.37(3)			
59415.4		12.4(2)			
59417.4	12.65(2)	12.56(2)	13.22(2)		
59417.9				14.67(8)	
59418.4	12.76(2)	12.49(2)			
59422.4	13.13(2)	12.95(2)	13.39(2)		
59423.4	13.24(2)	12.98(2)	13.37(2)		
59424.4	13.5(2)	13.01(2)	13.29(2)		
59425.4	13.63(2)	13.09(2)			
59426.4	13.66(2)	13.04(2)			
59427.4	13.78(2)	13.06(2)	13.18(2)		
59428.4	13.86(2)	13.06(2)			
59429.4	14.15(2)	13.17(2)	13.15(2)		
59430.4		13.22(2)	13.21(2)		
59434.4		13.55(2)	13.43(2)		
59435.4	14.71(2)	13.73(2)	13.52(2)		
59436.4	14.74(2)	13.74(2)	13.59(2)		
59438.4	14.86(2)	13.91(2)			
59439.4	14.98(2)	13.99(2)	13.82(2)		
59440.4	15.0(2)				
59442.4	15.06(2)		14.03(2)		
59443.4	15.06(2)	14.27(2)			
59444.4	15.13(2)				
59446.4	15.2(2)	14.43(2)	14.31(2)		
59447.4			14.34(2)		
59448.4	15.27(2)				
59449.4	15.22(2)		14.39(2)		
59450.4	15.29(2)	14.52(2)	14.55(2)		
59451.4		14.59(2)			
59452.4	15.32(2)	14.68(2)			
59453.4	15.39(2)	14.66(2)	14.63(2)		
59454.4	15.48(2)	14.67(2)	14.62(2)		
59455.4			14.72(2)		
59456.4	15.45(2)				
59458.4		14.85(2)	14.85(2)		
59459.4	15.53(2)	14.91(2)	14.9(2)		

MJD	ZTF*g*	ZTF*r*	ZTF*i*
59460.4	15.56(2)	14.96(2)	15.04(2)
59461.4	15.58(2)	14.96(2)	15.03(2)
59462.4	15.64(2)		15.09(2)
59463.4	15.61(2)	15.04(2)	
59464.4	15.61(2)	15.08(2)	15.16(2)
59465.4	15.67(2)	15.11(2)	15.16(2)
59467.4	15.67(2)	15.17(2)	
59468.4			15.34(2)
59469.4		15.25(2)	
59471.4		15.35(2)	15.5(2)
59474.4	15.8(2)	15.43(2)	15.63(2)
59476.4	15.84(2)	15.49(2)	
59477.4			15.71(2)
59478.4	15.88(2)	15.59(2)	
59480.4	15.9(2)	15.63(2)	15.87(2)
59484.4			15.91(2)
59485.4	16.0(2)	15.83(2)	
59487.4	16.04(2)	15.91(2)	16.13(2)
59489.4	16.06(2)	15.97(2)	
59491.4			16.22(2)
59494.4	16.17(2)	16.18(2)	16.38(2)
59497.4			16.52(2)
59498.4	16.22(2)		
59502.4	16.36(2)	16.46(2)	16.64(2)
59504.4	16.32(2)	16.39(2)	
59505.4			16.73(2)
59509.4			16.76(2)
59512.4	16.46(2)	16.67(2)	16.9(2)
59517.4			17.02(2)
59518.4	16.62(2)		
59520.4			17.14(3)
59521.4	16.67(2)	16.96(2)	
59523.4	16.77(2)		17.22(3)
59525.4	16.82(2)	17.02(2)	
59526.4			17.25(3)
59527.4	16.78(2)	17.1(2)	
59529.4			17.43(4)
59530.4		17.19(2)	
59532.4	16.86(2)		17.41(3)
59537.4	16.95(2)	17.42(3)	
59540.4	17.02(2)	17.57(3)	
59542.4			17.72(5)
59550.4			17.72(5)

Table A2. Correction values for the photometry and spectra of SN 2011fe, SN 2021rhu and SN 1986G, along with the Phillips relation parameter space measurements for those objects and SN 1991bg. It is noted that $R_V = 3.1$ was used for the MW extinction correction and $R_V = 2.57^{+0.23}_{-0.21}$ was used for the host correction of SN 1986G. *a* : Schlegel et al. (1998), *b* : Phillips et al. (2013b), *c* : Ferrarese et al. (2007), *d* : Phillips et al. (1999), *e* : Phillips et al. (1987), *f* : Turatto et al. (1996), *g* : Shappee & Stanek (2011), *h* : Richmond & Smith (2012), *i* : Dhawan et al. (2022).

Target	MW A_V	Host A_V	μ	$\Delta m_{B,15}$	$M_{B,\mathrm{peak}}$
SN 1986G	0.3054 ± 0.0016 $_a$	$2.03^{+0.09}_{-0.03}$ $_b$	27.67 ± 0.12 (Cepheid) $_c$	1.73 ± 0.07 $_d$	-18.24 ± 0.13 $_e$
SN 1991bg				1.95 ± 0.14 $_f$	-16.54 ± 0.32 $_f$
SN 2011fe	0.0239 ± 0.0006 $_a$		29.04 ± 0.05 (Cepheid) $_g$	1.21 ± 0.03 $_h$	-19.21 ± 0.15 $_h$
SN 2021rhu	0.1187 ± 0.0009 $_a$		30.86 ± 0.07 (TRGB) $_i$	1.45 ± 0.2	-18.59 ± 0.2

Table A3. Observational details for the spectral data of SN 2021rhu. The wavelength ranges specified are given after correcting the spectra to the rest from of the supernova.

MJD	Phase (d)	Telescope	Instrument	Observer	Reducer	Wavelength range (Å)
59398.37	-12.2	VLT	XShooter	*M. Bulla*	*K. Maguire*	3089-24705
59399.37	-11.2	VLT	XShooter	*M. Bulla*	*K. Maguire*	3089-24705
59400.37	-10.2	P60	SEDM	*ZTF*	-	3789-9191
59402.37	-8.2	VLT	XShooter	*M. Bulla*	*K. Maguire*	3789-9191
59403.17	-7.4	LT	SPRAT	*M. Deckers*	*M. Deckers*	4015-7966
59405.19	-5.4	LT	SPRAT	*M. Deckers*	*M. Deckers*	4015-7966
59409.15	-1.4	LT	SPRAT	*M. Deckers*	*M. Deckers*	4015-7966
59411.16	0.6	LT	SPRAT	*M. Deckers*	*M. Deckers*	4015-7966
59416.18	5.6	LT	SPRAT	*M. Deckers*	*J. Terwel*	4015-7966
59421.19	10.6	LT	SPRAT	*M. Deckers*	*M. Deckers*	4015-7966
59423.09	12.5	NOT	ALFOSC	*J. Sollerman, S. Schulze*	*S. Schulze*	3492-9516
59426.22	15.6	LT	SPRAT	*M. Deckers*	*M. Deckers*	4015-7966
59434.10	23.5	LT	SPRAT	*M. Deckers*	*M. Deckers*	4015-7966
59466.96	56.4	LT	SPRAT	*M. Deckers*	*M. Deckers*	4015-7966
59467.21	56.6	P60	SEDM	*ZTF*	-	3789-9191
59476.35	67.8	P60	SEDM	*ZTF*	-	3789-9191
59487.41	76.8	P60	SEDM	*ZTF*	-	3789-9191
59508.26	97.7	P60	SEDM	*ZTF*	-	3789-9191